Computer Methods in Applied Mechanics and Engineering 449 (2026) 118507

Contents lists available at ScienceDirect

Comput. Methods Appl. Mech. Engrg.

journal homepage: www.elsevier.com/locate/cma

Topology optimization of 3D finite deformation frictional mortar contact problems using adjoint sensitivities

L. Rinderer [a], A. Popp [b], M. W. Gee [a,*]

[a] Mechanics & High Performance Computing Group, Technical University of Munich, Parkring 35, Garching b. München, 85748, Germany
[b] Institute for Mathematics and Computer-Based Simulation, University of the Bundeswehr, Werner-Heisenberg-Weg 39, Neubiberg, 85577, Germany

ARTICLE INFO

Keywords:
Finite deformations
Mortar methods
Frictional contact mechanics
Sensitivity analysis
Adjoint method
Topology optimization

ABSTRACT

Gradient-based optimization strategies, such as topology optimization, rely on sensitivity information to iteratively update design parameters and optimize a performance measure. Advanced sensitivity analysis techniques, such as the adjoint method, leverage detailed knowledge of the system's governing equations. In the context of finite deformation contact mechanics, as considered here, both geometric nonlinearity and nonlinearity arising from the contact itself must be taken into account. When frictional sliding is present, the governing equations become path-dependent. In this contribution, we derive the sensitivity analysis within an adjoint framework, including consistent analytical linearization, for three of the most common contact constraint enforcement methods: the Lagrange multiplier method, the penalty method, and the augmented Lagrangian method. A state-of-the-art mortar finite element approach is used for the spatial discretization of contact and frictional sliding terms. Finally, we present numerical examples that demonstrate the capabilities of the newly developed sensitivity analysis strategies.

1. Introduction

Gradient-based minimization methods, commonly employed in optimization and inverse analysis, rely on accurate sensitivity information. As a result, techniques for computing sensitivities—such as direct differentiation or the adjoint approach—are of substantial interest. The complexity of such analyses is strongly influenced by the structure of the system's governing equations. In the context of finite deformation contact mechanics, both geometric nonlinearities and nonlinearities introduced through the enforcement of contact constraints must be accounted for. In problems involving frictional contact, the governing equations exhibit path-dependence, which necessitates that the entire loading history be incorporated into the sensitivity analysis.

Here, we present a consistent sensitivity analysis for 3D finite deformation frictional contact mechanics problems. A state-of-the-art mortar finite element approach is employed for the spatial discretization of contact and frictional sliding terms. The contact constraints are enforced using all three most common enforcement approaches, i.e. the Lagrange multiplier method (LMM), the penalty method (PM) and the augmented Lagrangian method (ALM). Since topology optimization is chosen as the representative application, we present the sensitivity analysis using the adjoint method, which is computationally more efficient than direct differentiation—though more memory-intensive—due to the typically large number of design parameters relative to the number of objective functions. Nevertheless, the methodology presented in this contribution can straightforwardly be transferred to the direct differentiation approach. The "time-discrete" variant of the adjoint method is employed, which ensures that consistent sensitivities are found [1]. To our knowledge, this is the first publication presenting topology optimized structures using consistent sensitivities for the described setting.

* Corresponding author.
E-mail addresses: lukas.rinderer@tum.de (L. Rinderer), alexander.popp@unibw.de (A. Popp), gee@tum.de (M.W. Gee).

https://doi.org/10.1016/j.cma.2025.118507
Received 7 April 2025; Received in revised form 17 October 2025; Accepted 18 October 2025
Available online 16 November 2025

In the LMM, the system is solved for the displacements and Lagrange multipliers simultaneously. The normal and tangential contact constraints are reformulated using nonlinear complementarity functions. Therefore, the forward problem can be solved using a semi-smooth Newton method. When constructing the adjoint problem for a specific time step, the converged tangent operator from the forward problem at that time step can be directly utilized. The PM utilizes a regularization which enables us to formulate the frictional contact problem in displacement variables only. To derive the sensitivity, the regularized contributions need to be linearized consistently, which is presented as well. The ALM combines the LMM and the PM, by introducing additional Lagrange multipliers and penalizing any violated constraint. In practice, two different approaches to implement the ALM exist. One possibility, which is known as the direct ALM, is to keep the Lagrange multipliers as additional unknowns and apply a standard Newton-Raphson scheme to solve the nonlinear problem. More commonly an Uzawa type algorithm is utilized to iteratively determine the Lagrange multiplier values. In this publication the iterative ALM is chosen. Either way, the contact constraints can be fulfilled exactly (direct ALM) or at least down to a user-defined accuracy threshold (iterative ALM), which allows us to construct a saddle-point-type system for the sensitivity analysis, similar to the LMM sensitivity analysis. Consequently, there is no need for an iterative scheme in the sensitivity analysis independent of the choice of contact enforcement approach.

In recent years, several publications on the sensitivity analysis of contact problems using various discretization problems have been published. For an extensive overview, we refer to Fernandez et al. [2].

Lawry and Maute combined the extended finite element method with an explicit level set function to optimize small [3] and finite deformation [4] frictionless contact of multiple deformable bodies. Meanwhile, Strömberg [5] presented an approach utilizing small deformation mortar frictionless contact with an ALM to topology optimize multiple deformable bodies. Fernandez et al. [2] presented topology optimization for 3D finite deformation frictionless mortar contact with an ALM. Recently, Sjövall et al. [6] used a shape optimization approach for 2D finite deformation frictionless mortar contact with an ALM.

Strömberg [7] introduced an approach using a smooth approximation to Signorini's contact to optimize small deformation frictional contact problems with topology optimization. Myśliński [8,9] combined the level set method with topological derivatives and optimized small deformation frictional contact problems using shape and topology optimization. Stupkiewicz et al. [10] presented the path-dependent shape sensitivity analysis using direct differentiation for a 2D finite deformation frictional contact problem using a node-to-segment approach and penalty regularization. Later, Stupkiewicz et al. [11] extended their node-to-segment approach to 3D finite deformation frictional contact with an ALM, where the sensitivities are derived using automatic differentiation. Niu et al. [12] presented the path-dependent sensitivity analysis for 2D small deformation node-to-node frictional contact mechanics using the PM.

Kristiansen et al. [13] presented a topology optimization approach considering linear elastic, frictional contact for 2D elastic-rigid problems. Therein, a Lagrange multiplier based contact formulation with non-smooth complementarity conditions is used to formulate a coupled Newton solution scheme [14]. The approach is extended to 2D, dynamic, finite deformation, frictional, elastic-rigid problems in [15]. In [15] the "time-continous" or "differentiate-then-discretize" variant of the adjoint method is used, which leads to small consistency errors in the sensitivity calculations, as stated in [1].

For an introduction to contact modeling and the related computational techniques, we refer to Laursen [16] and Wriggers [17]. Specifically, here we use segment-to-segment mortar finite element discretization as presented by Puso and Laursen [18,19]. The formulation of the semi-smooth Newton method follows Hüeber and Wohlmuth [20]. Its extension to finite deformation contact is introduced in Popp et al. [21,22]. A further extension to finite deformation frictional contact including an objective measure for the relative sliding velocity is presented in Gitterle et al. [23].

The outline of this paper is as follows. In Section 2, the terminology and definitions for the finite deformation mortar contact problem are introduced. The contact enforcement strategies LMM, PM and ALM are presented as briefly as possible. For more elaborate descriptions we refer to [21–23]. In Section 3, the adjoint method for general path-dependent systems is presented first. Afterward, it is applied to the frictional contact problem using the three introduced contact constraint enforcement strategies. Section 4 presents the density-based topology optimization formulation for finite deformation problems involving frictional contact, employing a mortar discretization. Numerical examples that demonstrate the application of the proposed sensitivity analysis strategies are provided in Section 5. Finally, conclusions are drawn in Section 6.

2. Forward problem

2.1. 3D finite deformation contact problem

For completeness and introduction of notation 3D finite deformation frictional contact using mortar discretization is briefly repeated, see Fig. 1. We consider two elastic bodies, represented by $\Omega_0^{(i)} \subset \mathbb{R}^3$, $i = 1, 2$, in the reference configuration, and correspondingly by $\Omega_t^{(i)} \subset \mathbb{R}^3$ in the current configuration. The surfaces $\partial\Omega^{(i)}$ include the Dirichlet boundary $\Gamma_u^{(i)}$, the Neumann boundary $\Gamma_\sigma^{(i)}$ and the potential contact boundary $\Gamma_{\text{co}}^{(i)}$, where contact constraints are enforced. The spatial counterparts are denoted by $\gamma_u^{(i)}$, $\gamma_\sigma^{(i)}$ and $\gamma_{\text{co}}^{(i)}$. The three surface sets are assumed to be disjoint, satisfying

$$\partial\Omega^{(i)} = \Gamma_u^{(i)} \cup \Gamma_\sigma^{(i)} \cup \Gamma_{\text{co}}^{(i)} \qquad \text{and} \qquad \Gamma_u^{(i)} \cap \Gamma_\sigma^{(i)} = \Gamma_u^{(i)} \cap \Gamma_{\text{co}}^{(i)} = \Gamma_\sigma^{(i)} \cap \Gamma_{\text{co}}^{(i)} = \emptyset \ . \tag{1}$$

Common nomenclature in contact mechanics refers to $\Gamma_{\text{co}}^{(1)}$ the slave and $\Gamma_{\text{co}}^{(2)}$ the master surface. Contact is modeled using normal (non-penetration) and tangential (frictional sliding) constraints. We limit ourselves to Coulomb friction for ease of discussion.

The coordinates in reference and current configuration are denoted by $\boldsymbol{X}^{(i)} \in \mathbb{R}^3$ and $\boldsymbol{x}^{(i)} \in \mathbb{R}^3$. The projection of $\boldsymbol{x}^{(1)}$ onto the master surface $\gamma_{\text{co}}^{(2)}$ along $\boldsymbol{n}$ is denoted by $\hat{\boldsymbol{x}}^{(2)} \in \mathbb{R}^3$. It's corresponding counterpart in the reference configuration is $\hat{\boldsymbol{X}}^{(2)} \in \mathbb{R}^3$. The

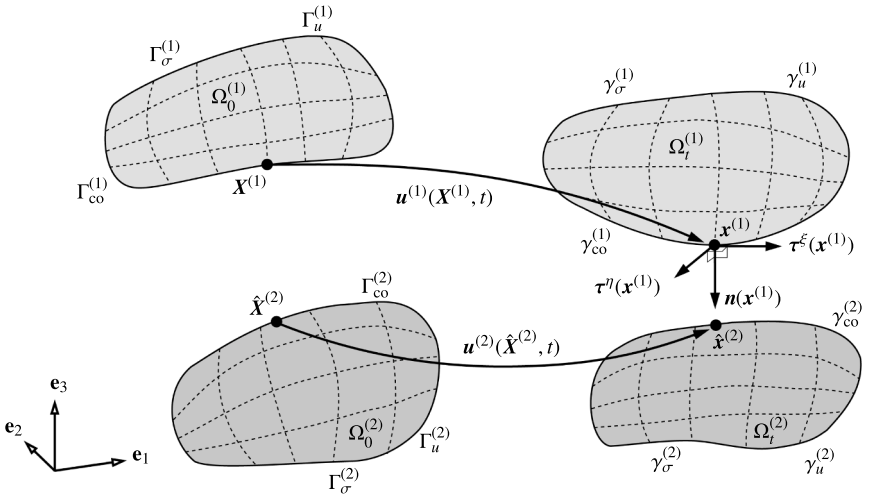

Fig. 1. Notation for the three-dimensional two body finite deformation contact problem, based on [24].

current configuration outward unit normal on the slave surface is $\boldsymbol{n} \in \mathbb{R}^3$. The tangential plane to the slave surface $\boldsymbol{\tau} \in \mathbb{R}^{3\times 2}$, $\boldsymbol{\tau} := \left[\boldsymbol{\tau}^\xi \ \boldsymbol{\tau}^\eta\right]^T$ in the current configuration is spanned by the orthonormal vectors $\boldsymbol{\tau}^\xi, \boldsymbol{\tau}^\eta \in \mathbb{R}^3$. Together $\boldsymbol{n}$ and $\boldsymbol{\tau}$ form an orthonormal basis in $\boldsymbol{x}^{(1)}$. The deformation of both bodies is described by the absolute displacement vectors $\boldsymbol{u}^{(i)} \in \mathbb{R}^3$, satisfying $\boldsymbol{x}^{(i)} = \boldsymbol{X}^{(i)} + \boldsymbol{u}^{(i)}$. In the current configuration, we define the gap vector, that is the relative position of slave and master surface to each other, as

$$\boldsymbol{g} = \boldsymbol{x}^{(1)} - \hat{\boldsymbol{x}}^{(2)} \ . \tag{2}$$

Additionally, the scalar valued normal gap is defined as

$$g_{\text{n}} = -\boldsymbol{n} \cdot \boldsymbol{g} \ , \tag{3}$$

and the relative tangential velocity of $\boldsymbol{x}^{(1)}$ and $\hat{\boldsymbol{x}}^{(2)}$ as

$$\boldsymbol{v}_{\tau,\text{rel}} = \boldsymbol{\tau} \cdot \left[\dot{\boldsymbol{x}}^{(1)} - \dot{\hat{\boldsymbol{x}}}^{(2)}\right] \ . \tag{4}$$

The contact tractions in the current configuration on the slave surface can be decomposed into normal and tangential components

$$\boldsymbol{t}_{\text{co}}^{(1)} = p_{\text{n}}\boldsymbol{n} + t_\tau^\xi \boldsymbol{\tau}^\xi + t_\tau^\eta \boldsymbol{\tau}^\eta \ , \quad p_{\text{n}} = \boldsymbol{t}_{\text{co}}^{(1)} \cdot \boldsymbol{n} \ , \quad t_\tau^\xi = \boldsymbol{t}_{\text{co}}^{(1)} \cdot \boldsymbol{\tau}^\xi \ , \quad t_\tau^\eta = \boldsymbol{t}_{\text{co}}^{(1)} \cdot \boldsymbol{\tau}^\eta \ , \tag{5}$$

where we summarize the tangential components of the contact traction into the two component vector $\boldsymbol{t}_\tau := \left[t_\tau^\xi \ t_\tau^\eta\right]^T$. The Hertz-Signorini-Moreau (HSM) conditions formulate the contact constraints in normal direction as

$$g_{\text{n}} \geq 0 \ , \quad p_{\text{n}} \leq 0 \ , \quad p_{\text{n}} g_{\text{n}} = 0 \ . \tag{6}$$

According to Coulomb's friction law, the contact constraints in tangential direction are

$$\varphi := \|\boldsymbol{t}_\tau\| - \mu\,|p_{\text{n}}| \leq 0 \ , \qquad \boldsymbol{v}_{\tau,\text{rel}} + \beta\,\boldsymbol{t}_\tau = \boldsymbol{0} \ , \qquad \beta \geq 0 \ , \qquad \varphi\,\beta = 0 \ , \tag{7}$$

where $\|\cdot\|$ denotes the L_2-norm in $\mathbb{R}^3$, $\mu \geq 0$ is the friction coefficient and β is a scalar parameter.

We introduce the Lagrange multiplier vector $\boldsymbol{\lambda} = -\boldsymbol{t}_{\text{co}}^{(1)}$, which represents the negative slave side traction $\boldsymbol{t}_{\text{co}}^{(1)}$. It is chosen from a suitable solution space denoted by $\mathcal{M}(\lambda)$, see [25] for details, such that the contact constraints (6) and (7) are satisfied in a weak sense.

A key feature of the mortar method is to introduce a weak, integral form of the contact conditions, contrary to the strong, pointwise formulations as used in e.g. node-to-segment approaches. We extend the standard weak form of nonlinear solid mechanics to two subdomains and combine it with the Lagrange multiplier coupling terms. The weak saddle point formulation is: Find $\boldsymbol{u}^{(i)} \in \mathcal{U}^{(i)}$ and $\boldsymbol{\lambda} \in \mathcal{M}(\lambda)$ such that

$$\delta\Pi_{\text{int,ext}}(\boldsymbol{u}^{(i)}, \delta\boldsymbol{u}^{(i)}) + \delta\Pi_{\text{co}}(\boldsymbol{\lambda}, \delta\boldsymbol{u}^{(i)}) = 0 \qquad \forall \delta\boldsymbol{u}^{(i)} \in \mathcal{V}^{(i)} \ , \tag{8}$$

$$\delta\Pi_\lambda(\boldsymbol{u}^{(i)}, \delta\boldsymbol{\lambda}) \geq 0 \qquad \forall \delta\boldsymbol{\lambda} \in \mathcal{M}(\lambda) \ , \tag{9}$$

where $\mathcal{U}^{(i)}$ and $\mathcal{V}^{(i)}$ denote the usual solution and weighting spaces. Herein, the internal and external contributions $\delta\Pi_{\text{int,ext}}$ are the standard nonlinear solid mechanics virtual work contributions. The contact contributions $\delta\Pi_{\text{co}}$ and the weak constraints $\delta\Pi_\lambda$, including non-penetration and frictional sliding conditions, are given as

$$\delta\Pi_{\text{co}}(\boldsymbol{\lambda}, \delta\boldsymbol{u}^{(i)}) = \int_{\gamma_{\text{co}}^{(1)}} \boldsymbol{\lambda} \cdot \left(\delta\boldsymbol{u}^{(1)} - \delta\boldsymbol{u}^{(2)} \circ \chi\right) \mathrm{d}\gamma \ , \tag{10}$$

$$\delta\Pi_\lambda(\boldsymbol{u}^{(i)}, \delta\boldsymbol{\lambda}) = \int_{\gamma_{\text{co}}^{(1)}} (\delta\lambda_{\text{n}} - \lambda_{\text{n}}) g_{\text{n}} \mathrm{d}\gamma - \int_{\gamma_{\text{co}}^{(1)}} (\delta\boldsymbol{\lambda}_\tau - \boldsymbol{\lambda}_\tau) \cdot \boldsymbol{v}_{\tau,\text{rel}} \mathrm{d}\gamma \ , \tag{11}$$

where $\chi : \gamma_{\mathrm{co}}^{(1)} \to \gamma_{\mathrm{co}}^{(2)}$ denotes a suitable map from slave to master side of the contact surface [26]. Note that χ continuously changes due to a relative movement of slave and master surfaces, i.e. it depends on the displacements $\boldsymbol{u}^{(i)}$.

2.2. Discretization

We consider a quasi-static problem with N load steps, load step count (pseudo time) t_n, with $n = 1, \dots, N$. For simplicity, we assume a constant time increment $\Delta t = t_n - t_{n-1}$, throughout simulations. For the spatial discretization of the two deformable bodies $\Omega^{(i)}$, we use standard 3D Lagrangian finite elements. All finite element nodes in the two discretized domains $\Omega_h^{(i)}$ are split into three subsets: a subset $\mathcal{S}$ containing all n_{sl} slave side contact nodes, a subset $\mathcal{M}$ of all n_{m} master side contact nodes and the set of all remaining nodes $\mathcal{N}$. Here the focus is set on the finite element discretization of the coupling terms. The geometry interpolation on $\Gamma_{\mathrm{co},h}^{(i)}$ is given by

$$\boldsymbol{x}_h^{(1)}|_{\Gamma_{\mathrm{co},h}^{(1)}} = \sum_{k=1}^{n_{\mathrm{sl}}} N_k^{(1)}\big(\xi^{(1)}, \eta^{(1)}\big)\boldsymbol{x}_k^{(1)} \quad , \qquad \boldsymbol{x}_h^{(2)}|_{\Gamma_{\mathrm{co},h}^{(2)}} = \sum_{l=1}^{n_{\mathrm{m}}} N_l^{(2)}\big(\xi^{(2)}, \eta^{(2)}\big)\boldsymbol{x}_l^{(2)} \quad , \tag{12}$$

where the discrete nodal positions $\boldsymbol{x}_k^{(1)}$, $\boldsymbol{x}_l^{(2)}$ are introduced. For the displacement field the same isoparametric approximation is used, introducing the discrete nodal displacements $\boldsymbol{d}_k^{(1)}$, $\boldsymbol{d}_l^{(2)}$. The shape functions $N_k^{(1)}$ and $N_l^{(2)}$ are defined with respect to the usual finite element parameter space. The discretization of the Lagrange multiplier vector is

$$\boldsymbol{\lambda}_h = \sum_{j=1}^{n_{\mathrm{sl}}} \Phi_j\big(\xi^{(1)}, \eta^{(1)}\big)\boldsymbol{z}_j \quad , \tag{13}$$

with the shape functions Φ_j and the nodal values of the Lagrange multiplier field $\boldsymbol{z}_j \in \mathbb{R}^3$. Often two different families of discrete Lagrange multipliers, namely standard and so-called dual Lagrange multipliers, are distinguished. In standard mortar methods the identical shape functions are utilized for Lagrange multiplier and slave displacement interpolation, i.e. $\Phi_j = N_j^{(1)}$. Dual shape functions are constructed such that a so-called biorthogonality condition is fulfilled [20,27]. We write the discrete version of the contact virtual work expression (10) as

$$\Pi_{\mathrm{co},h} = \sum_{j=1}^{n_{\mathrm{sl}}}\sum_{k=1}^{n_{\mathrm{sl}}} \boldsymbol{z}_j{}^T\left(\int_{\gamma_{\mathrm{co},h}^{(1)}} \Phi_j\, N_k^{(1)}\mathrm{d}\gamma\right)\delta\boldsymbol{d}_k^{(1)} - \sum_{j=1}^{n_{\mathrm{m}}}\sum_{l=1}^{n_{\mathrm{sl}}} \boldsymbol{z}_j{}^T\left(\int_{\gamma_{\mathrm{co},h}^{(1)}} \Phi_j\,(N_l^{(2)} \circ \chi_h)\,\mathrm{d}\gamma\right)\delta\boldsymbol{d}_l^{(2)} \quad , \tag{14}$$

with the discrete nodal virtual displacements $\delta\boldsymbol{d}_k^{(1)}, \delta\boldsymbol{d}_l^{(2)}$ and the discrete contact mapping $\chi_h : \gamma_{\mathrm{co},h}^{(1)} \to \gamma_{\mathrm{co},h}^{(2)}$. Herein we identify nodal blocks of the two mortar integral matrices $\mathbf{D} \in \mathbb{R}^{3n_{\mathrm{sl}} \times 3n_{\mathrm{sl}}}$ and $\mathbf{M} \in \mathbb{R}^{3n_{\mathrm{sl}} \times 3n_{\mathrm{m}}}$

$$\mathbf{D}[j,j] = \int_{\gamma_{\mathrm{co},h}^{(1)}} \Phi_j\, N_k^{(1)}\mathrm{d}\gamma\, \boldsymbol{I} \quad , \qquad \mathbf{M}[j,l] = \int_{\gamma_{\mathrm{co},h}^{(1)}} \Phi_j\,(N_l^{(2)} \circ \chi_h)\mathrm{d}\gamma\, \boldsymbol{I} \quad , \tag{15}$$

with the identity matrix $\boldsymbol{I} \in \mathbb{R}^{3x3}$. Using the three introduced subsets $\mathcal{N}$, $\mathcal{M}$ and $\mathcal{S}$ the discrete nodal displacements are summarized into the discrete global displacement vector $\boldsymbol{d} = (\boldsymbol{d}_{\mathcal{N}}, \boldsymbol{d}_{\mathcal{M}}, \boldsymbol{d}_{\mathcal{S}})^T$. The global virtual displacement vector $\delta\boldsymbol{d}$ is constructed accordingly. Thus, the discrete contact virtual work (14) can be reformulated as

$$\Pi_{\mathrm{co},h} = \delta\boldsymbol{d}^T[\mathbf{0} \;\; -\mathbf{M}(\boldsymbol{d}) \;\; \mathbf{D}(\boldsymbol{d})]^T\boldsymbol{z} = \delta\boldsymbol{d}^T\boldsymbol{f}_{\mathrm{co}}(\boldsymbol{d},\boldsymbol{z}) \quad , \tag{16}$$

where $\boldsymbol{z} \in \mathbb{R}^{3n_{\mathrm{sl}}}$ is the assembled vector of all nodal values of the Lagrange multiplier field. Here we introduced the vector of discrete contact forces $\boldsymbol{f}_{\mathrm{co}} \in \mathbb{R}^{n_{\mathrm{dof}}}$ as

$$\boldsymbol{f}_{\mathrm{co}}(\boldsymbol{d},\boldsymbol{z}) = [\mathbf{0} \;\; -\mathbf{M}(\boldsymbol{d}) \;\; \mathbf{D}(\boldsymbol{d})]^T\boldsymbol{z} \quad . \tag{17}$$

Discretization of the remaining contributions to (8) is not discussed, but the reader is instead referred to the abundant literature. Following [23] we can formulate the discrete force residual as

$$\boldsymbol{R} = \boldsymbol{f}_{\mathrm{int}}(\boldsymbol{d}) + \boldsymbol{f}_{\mathrm{co}}(\boldsymbol{d},\boldsymbol{z}) - \boldsymbol{f}_{\mathrm{ext}} = \mathbf{0} \quad , \tag{18}$$

with vectors of internal and external forces, $\boldsymbol{f}_{\mathrm{int}} \in \mathbb{R}^{n_{\mathrm{dof}}}$ and $\boldsymbol{f}_{\mathrm{ext}} \in \mathbb{R}^{n_{\mathrm{dof}}}$. The internal forces $\boldsymbol{f}_{\mathrm{int}}$ depend nonlinearly on the discretized displacements vector $\boldsymbol{d} \in \mathbb{R}^{n_{\mathrm{dof}}}$ due to the finite deformations involved. The nodal values of the Lagrange multiplier field can be decomposed into normal and tangential nodal contribution as

$$\boldsymbol{z}(\boldsymbol{d}) = \mathop{\mathsf{A}}_{j\in\mathcal{S}} \boldsymbol{n}_j\, z_{\mathrm{n}j} + \boldsymbol{\tau}_j\, \boldsymbol{z}_{\tau j} \quad , \tag{19}$$

where A is the assembly operator and $z_{\mathrm{n}j} \in \mathbb{R}$ and $\boldsymbol{z}_{\tau j} \in \mathbb{R}^2$ are the projections of the nodal Lagrange multiplier $\boldsymbol{z}_j$ in the normal direction and onto the tangential plane

$$z_{\mathrm{n}j} = \boldsymbol{n}_j^T\boldsymbol{z}_j \qquad \text{and} \qquad \boldsymbol{z}_{\tau j} = \boldsymbol{\tau}_j^T\boldsymbol{z}_j \quad . \tag{20}$$

In addition to the discrete force residual (18), contact constraints are required, for details see [21,23]. Discrete conditions of the nodal, normal contact constraints (HSM conditions) for each slave node $j \in \mathcal{S}$ are

$$\tilde{g}_j \geq 0 \qquad z_{\mathrm{n}j} \geq 0 \qquad z_{\mathrm{n}j}\,\tilde{g}_j = 0 \quad , \tag{21}$$

with the nodal weighted gap measure

$$\tilde{g}_j = -\boldsymbol{n}_j^T \mathbf{D}[j,j]\,\boldsymbol{x}_j^{(1)} + \boldsymbol{n}_j^T \sum_{l=1}^{n_\mathrm{m}} \mathbf{M}[j,l]\,\boldsymbol{x}_l^{(2)} \geq 0 \quad . \tag{22}$$

Discrete conditions of the nodal, tangential contact constraints (Coulomb's friction law) for each slave node $j \in \mathcal{S}$ are

$$\varphi_j := \|\boldsymbol{z}_{\tau j}\| - \mu\, z_{\mathrm{n}j} \leq 0 \tag{23a}$$

$$\tilde{\boldsymbol{v}}_{\tau j} + \beta_j\, \boldsymbol{z}_{\tau j} = \boldsymbol{0} \tag{23b}$$

$$\beta_j \geq 0 \tag{23c}$$

$$\varphi_j\, \beta_j = 0 \quad , \tag{23d}$$

where we introduced the slip condition φ_j, the tangential relative slip velocity $\tilde{\boldsymbol{v}}_{\tau j}$ and a frictional multiplier β_j. The time discrete nodal slip increment

$$\tilde{\boldsymbol{u}}_{\tau j}(t_n) = -\boldsymbol{\tau}_j^T(t_n)\big(\mathbf{D}[j,j](t_n) - \mathbf{D}[j,j](t_{n-1})\big)\boldsymbol{x}_j^{(1)}(t_n) + \boldsymbol{\tau}_j^T(t_n) \sum_{l=1}^{n_\mathrm{m}} \big(\mathbf{M}[j,l](t_n) - \mathbf{M}[j,l](t_{n-1})\big)\boldsymbol{x}_l^{(2)}(t_n) \tag{24}$$

is derived from the objectivity requirement of the tangential relative slip velocity $\tilde{\boldsymbol{v}}_{\tau j}$, see [23] for further details. Utilizing the relation $\tilde{\boldsymbol{u}}_{\tau j} = \tilde{\boldsymbol{v}}_{\tau j} \cdot \Delta t$, where Δt is the time increment, (23b) can be reformulated as $\tilde{\boldsymbol{u}}_{\tau j} + \tilde{\beta}_j\, \boldsymbol{z}_{\tau j} = \boldsymbol{0}$, where $\tilde{\beta} = \beta \cdot \Delta t$.

2.3. Lagrange multiplier method

2.3.1. Non-smooth complementarity functions

The contact constraints (21) and (23) are reformulated in so-called complementarity functions, such that a semi-smooth Newton-type algorithm can be applied not only for geometrical and material nonlinearity, but also for the nonlinearity stemming from contact [28]. As given and discussed in detail for small deformations in [20] and in the finite deformation context in [22], the complementarity function for the normal contact is defined for each slave node $j \in \mathcal{S}$ as

$$C_{\mathrm{n}j}(\boldsymbol{z}_j, \boldsymbol{d}) = z_{\mathrm{n}j} - \max\left(0, (z_{\mathrm{n}j} - c_\mathrm{n}\tilde{g}_j)\right) \qquad c_\mathrm{n} > 0 \tag{25}$$

and fulfills all three (in-)equality conditions in (21) when $C_{\mathrm{n}j}(\boldsymbol{z}_j, \boldsymbol{d}) = 0$ independently of the choice of c_n. The complementarity function for Coulomb's friction law (23) is given as tangential complementarity function for each slave node $j \in \mathcal{S}$ [23,25,29] as

$$\boldsymbol{C}_{\tau j}(\boldsymbol{z}_j, \boldsymbol{d}) = \max\left(\mu(z_{\mathrm{n}j} - c_\mathrm{n}\tilde{g}_j), \|\boldsymbol{z}_{\tau j} + c_\tau \tilde{\boldsymbol{u}}_{\tau j}\|\right)\boldsymbol{z}_{\tau j} - \mu \max\left(0, (z_{\mathrm{n}j} - c_\mathrm{n}\tilde{g}_j)\right)(\boldsymbol{z}_{\tau j} + c_\tau \tilde{\boldsymbol{u}}_{\tau j}) \qquad c_\mathrm{n} > 0, c_\tau > 0 \quad . \tag{26}$$

Coulomb's friction law with all the (in-)equalities expressed in (23) is equivalently expressed as $\boldsymbol{C}_{\tau j}(\boldsymbol{z}_j, \boldsymbol{d}) = \boldsymbol{0}$ independently of the choice of c_n and c_τ.

2.3.2. Semi-smooth Newton method as an active set strategy

Combining the discrete force residual (18) with the complementarity functions (25) and (26), the following nonlinear system of equations is obtained

$$\begin{aligned} \boldsymbol{R} = \boldsymbol{f}_\mathrm{int}(\boldsymbol{d}) + \boldsymbol{f}_\mathrm{co}(\boldsymbol{d}, \boldsymbol{z}) - \boldsymbol{f}_\mathrm{ext} &= \boldsymbol{0} \\ C_{\mathrm{n}j}(\boldsymbol{z}_j, \boldsymbol{d}) &= 0 \quad \forall j \in \mathcal{S} \\ \boldsymbol{C}_{\tau j}(\boldsymbol{z}_j, \boldsymbol{d}) &= \boldsymbol{0} \quad \forall j \in \mathcal{S} \quad . \end{aligned} \tag{27}$$

The complementarity functions (25) and (26) are non-smooth due to the *max*-function. Performing a semi-smooth Newton step at the current iterate k to be solved for the pair $(\boldsymbol{d}^{k+1}, \boldsymbol{z}^{k+1})$ yields

$$\begin{aligned} \Delta\boldsymbol{R}(\boldsymbol{d}^k, \boldsymbol{z}^k) &= -\boldsymbol{R}^k \\ \Delta C_{\mathrm{n}j}(\boldsymbol{d}^k, \boldsymbol{z}_j^k) &= -C_{\mathrm{n}j}^k \quad \forall j \in \mathcal{S} \\ \Delta\boldsymbol{C}_{\tau j}(\boldsymbol{d}^k, \boldsymbol{z}_j^k) &= -\boldsymbol{C}_{\tau j}^k \quad \forall j \in \mathcal{S} \end{aligned} \tag{28}$$

where

$$\Delta(\cdot) = \frac{\partial(\cdot)}{\partial \boldsymbol{d}}\Delta\boldsymbol{d} + \frac{\partial(\cdot)}{\partial \boldsymbol{z}}\Delta\boldsymbol{z} \quad . \tag{29}$$

Then, the update for the new iterate $(\boldsymbol{d}^{k+1}, \boldsymbol{z}^{k+1})$ is

$$(\boldsymbol{d}^{k+1}, \boldsymbol{z}^{k+1}) = (\boldsymbol{d}^k, \boldsymbol{z}^k) + (\Delta\boldsymbol{d}^k, \Delta\boldsymbol{z}^k) \quad . \tag{30}$$

The non-smooth complementarity functions (25) and (26) are utilized to differentiate the solution branches. Evaluating the directional derivative of the complementarity function $C_{\mathrm{n}j}$ yields the separation of the slave node set $\mathcal{S}$ into the inactive node set $\mathcal{I}$ and the active node set $\mathcal{A}$. The sets are divided by:

$$\mathcal{I} := \{j \in \mathcal{S} \mid z_{\mathrm{n}j} - c_\mathrm{n}\tilde{g}_j \leq 0\} \qquad \text{inactive set, nodes not in contact}$$

$$\mathcal{A} := \{j \in S \mid z_{\mathrm{n}j} - c_{\mathrm{n}} \tilde{g}_j > 0\} \qquad \text{active set, nodes in contact}$$

For $\mathcal{I}$ and $\mathcal{A}$ the normal nonlinear complementarity functions (25) reduce to

$$C_{\mathrm{n}j,\mathcal{I}}(\boldsymbol{z}_j, \boldsymbol{d}) = z_{\mathrm{n}j} \quad , \tag{31}$$

$$C_{\mathrm{n}j,\mathcal{A}}(\boldsymbol{z}_j, \boldsymbol{d}) = c_{\mathrm{n}}\, \tilde{g}_j \qquad c_{\mathrm{n}} > 0 \quad . \tag{32}$$

The tangential complementarity function $\boldsymbol{C}_{\tau j}$ contains the separation of the slave node set S into the inactive node set $\mathcal{I}$ and the active node set $\mathcal{A}$ as well. Additionally, the active set $\mathcal{A}$ is further split into the stick node set St and the slip node set Sl:

$$St := \{j \in \mathcal{A} \mid \|\boldsymbol{z}_{\tau j} + c_\tau \tilde{\boldsymbol{u}}_{\tau j}\| - \mu(z_{\mathrm{n}j} - c_{\mathrm{n}} \tilde{g}_j) < 0\} \qquad \text{stick set, nodes in contact and sticking}$$

$$Sl := \{j \in \mathcal{A} \mid \|\boldsymbol{z}_{\tau j} + c_\tau \tilde{\boldsymbol{u}}_{\tau j}\| - \mu(z_{\mathrm{n}j} - c_{\mathrm{n}} \tilde{g}_j) \geq 0\} \qquad \text{slip set, nodes in contact and slipping}$$

For St and Sl, the tangential nonlinear complementarity functions reduce to

$$\boldsymbol{C}_{\tau j,St}(\boldsymbol{z}_j, \boldsymbol{d}) = -\mu(z_{\mathrm{n}j} - c_{\mathrm{n}} \tilde{g}_j)\, c_\tau\, \tilde{\boldsymbol{u}}_{\tau j} \qquad c_{\mathrm{n}} > 0, c_\tau > 0 \quad , \tag{33}$$

$$\boldsymbol{C}_{\tau j,Sl}(\boldsymbol{z}_j, \boldsymbol{d}) = \|\boldsymbol{z}_{\tau j} + c_\tau \tilde{\boldsymbol{u}}_{\tau j}\|\, \boldsymbol{z}_{\tau j} - \mu(z_{\mathrm{n}j} - c_{\mathrm{n}} \tilde{g}_j)(\boldsymbol{z}_{\tau j} + c_\tau \tilde{\boldsymbol{u}}_{\tau j}) \qquad c_{\mathrm{n}} > 0, c_\tau > 0 \quad . \tag{34}$$

The assembly of all nodal nonlinear complementarity functions as contact residual is defined as

$$\boldsymbol{H}^k = \begin{bmatrix} \boldsymbol{C}^k_{\mathrm{n},\mathcal{I}}(\boldsymbol{z}, \boldsymbol{d}) \\ \boldsymbol{C}^k_{\mathrm{n},\mathcal{A}}(\boldsymbol{z}, \boldsymbol{d}) \\ \boldsymbol{C}^k_{\tau,St}(\boldsymbol{z}, \boldsymbol{d}) \\ \boldsymbol{C}^k_{\tau,Sl}(\boldsymbol{z}, \boldsymbol{d}) \end{bmatrix} = \boldsymbol{0} \quad . \tag{35}$$

We can rewrite the algebraic representation of the linear system (28) to be solved in each semi-smooth Newton step k

$$\begin{bmatrix} \dfrac{\partial \boldsymbol{R}^k}{\partial \boldsymbol{d}^k} & \dfrac{\partial \boldsymbol{R}^k}{\partial \boldsymbol{z}^k} \\ \dfrac{\partial \boldsymbol{H}^k}{\partial \boldsymbol{d}^k} & \dfrac{\partial \boldsymbol{H}^k}{\partial \boldsymbol{z}^k} \end{bmatrix} \begin{bmatrix} \Delta \boldsymbol{d}^k \\ \boldsymbol{z}^{k+1} \end{bmatrix} = - \begin{bmatrix} \boldsymbol{R}^k \\ \boldsymbol{H}^k \end{bmatrix} , \tag{36}$$

which results in an updated displacement field $\boldsymbol{d}^{k+1}$ and a set of Lagrange multipliers (contact forces) $\boldsymbol{z}^{k+1}$. The linearizations of the force residual $\boldsymbol{R}$ and the normal nonlinear complementarity function $\boldsymbol{C}_{\mathrm{n}}$ with respect to the primary variables $\boldsymbol{d}$ and $\boldsymbol{z}$ require the consistent linearization of several quantities including the mortar matrices $\mathbf{D}$ and $\mathbf{M}$, and consequently the discrete projection χ_h. All necessary linearizations are given in detail in [21,22]. For the linearization of the tangential complementarity function $\boldsymbol{C}_\tau$ we refer to [23].

2.4. Penalty method

We approximate the contact constraints (21) and (23) by introducing a penalty of any constraint violation instead. Similarly to the nodal values of the Lagrange multiplier field $\boldsymbol{z}_j$, we introduce a nodal discrete traction vector $\boldsymbol{t}_j$ with normal $\boldsymbol{t}_{\mathrm{n}j}$ and tangential $\boldsymbol{t}_{\tau j}$ contributions. For the normal HSM condition (21) the relationship of normal contact traction $t_{\mathrm{n}j}$ and gap measure $\tilde{g}_j$ is regularized by introducing a penalty parameter ϵ_{n}

$$t_{\mathrm{n}j} = \begin{cases} \epsilon_{\mathrm{n}}\, \tilde{g}_j & \text{if} \quad \tilde{g}_j \leq 0 \qquad \text{(contact)} \\ 0 & \text{else} \qquad\qquad\ \ \text{(no contact)} \quad . \end{cases} \tag{37}$$

To formulate the penalty regularized Coulomb's friction law, it is convenient to introduce the traction rate measure as

$$\mathcal{L}_v\, \boldsymbol{t}_{\tau j} = \epsilon_\tau \left[\tilde{\boldsymbol{v}}_{\tau j} - \beta \frac{\boldsymbol{t}_{\tau j}}{\|\boldsymbol{t}_{\tau j}\|} \right] \quad , \tag{38}$$

where $\mathcal{L}_v\, \boldsymbol{t}_{\tau j}$ is the Lie time derivative of the frictional traction and ϵ_τ the tangential penalty parameter. The Lie time derivative is necessary to maintain objectivity [30]. Coulomb's friction law is completed with (23a), (23c) and (23d).

The frictional evolution equations require a local time-stepping scheme, to obtain the tractions at step $n+1$. We apply a backward Euler integrator, accomplished via a trial state/return map algorithm. The reformulated tangential Karush-Kuhn-Tucker (KKT) conditions are

$$\begin{aligned} \varphi_{j,n+1} &:= \|\boldsymbol{t}_{\tau j,n+1}\| - \mu\, t_{\mathrm{n}j,n+1} \leq 0 \\ \boldsymbol{t}_{\tau j,n+1} &= \boldsymbol{t}_{\tau j,n} + \epsilon_\tau \left\{ \tilde{\boldsymbol{u}}_{\tau j,n+1} - \tilde{\beta} \frac{\boldsymbol{t}_{\tau j,n+1}}{\|\boldsymbol{t}_{\tau j,n+1}\|} \right\} \\ \tilde{\beta}_j &\geq 0 \\ \varphi_{j,n+1}\, \tilde{\beta}_j &= 0 \quad . \end{aligned} \tag{39}$$

Using penalty regularization, any additional variables (i.e. the Lagrange multipliers in the LMM case) are eliminated. The problem posed above is solely displacement driven; the updates for the frictional tractions are computed according to the geometric quantities

gap and relative slip. One computes a trial state, assuming no slip during the increment:

$$\begin{aligned} t_{\mathrm{n}j,n+1} &= \epsilon_{\mathrm{n}}\, \tilde{g}_{j,n+1} \\ \boldsymbol{t}^{\mathrm{trial}}_{\tau j,n+1} &= \boldsymbol{t}_{\tau j,n} + \epsilon_\tau\, \boldsymbol{\tau}_{j,n+1}\, \tilde{\boldsymbol{u}}_{\tau j,n+1} \\ \varphi^{\mathrm{trial}}_{j,n+1} &= \|\boldsymbol{t}^{\mathrm{trial}}_{\tau j,n+1}\| - \mu\, t_{\mathrm{n}j,n+1} \end{aligned} \tag{40}$$

The slip condition $\varphi^{\mathrm{trial}}_{j,n+1}$ then is checked. The tangential tractions $\boldsymbol{t}_{\tau j,n+1}$ are calculated based upon this determination:

$$\boldsymbol{t}_{\tau j,n+1} = \begin{cases} \boldsymbol{t}^{\mathrm{stick}}_{\tau j,n+1} = \boldsymbol{t}^{\mathrm{trial}}_{\tau j,n+1} & \text{if } \varphi^{\mathrm{trial}}_{j,n+1} \le 0 \quad \text{(stick)} \\ \boldsymbol{t}^{\mathrm{slip}}_{\tau j,n+1} = \boldsymbol{t}^{\mathrm{trial}}_{\tau j,n+1} \frac{\mu\, t_{\mathrm{n}j,n+1}}{\|\boldsymbol{t}^{\mathrm{trial}}_{\tau j,n+1}\|} & \text{else} \quad \text{(slip)} \ . \end{cases} \tag{41}$$

Assemble the global traction vector as

$$\boldsymbol{t}_{n+1} = \mathop{\mathsf{A}}_{j\in\mathcal{S}} t_{\mathrm{n}j,n+1}\, \boldsymbol{n}_{j,n+1} + \boldsymbol{t}_{\tau j,n+1} \ . \tag{42}$$

Utilizing the two global mortar coupling matrices, the contact forces follow as

$$\boldsymbol{f}_{\mathrm{co},n+1} = \begin{bmatrix} \boldsymbol{0} & -\boldsymbol{M}_{n+1} & \boldsymbol{D}_{n+1} \end{bmatrix}^T \boldsymbol{t}_{n+1} \ . \tag{43}$$

The discrete force residual (18) is now formulated with displacement degrees of freedom only

$$\boldsymbol{R}_{n+1} = \boldsymbol{f}_{\mathrm{int},n+1}(\boldsymbol{d}) + \boldsymbol{f}_{\mathrm{co},n+1}(\boldsymbol{d}) - \boldsymbol{f}_{\mathrm{ext},n+1} = \boldsymbol{0} \ . \tag{44}$$

Therefore, the algebraic representation of the linear system to be solved in each Newton step k is

$$\frac{\partial \boldsymbol{R}}{\partial \boldsymbol{d}} \Delta \boldsymbol{d} = -\boldsymbol{R} \ . \tag{45}$$

For the details on linearization of the regularized contact force we refer to [16].

2.5. Augmented Lagrangian method

In the ALM additional Lagrange multipliers, as in the LMM, are introduced. Furthermore, any violation of the contact constraints, (21) and (23), is penalized using a regularization as in the PM. We use an Uzawa type algorithm to iteratively approximate the Lagrange multipliers.

The normal contact traction is evaluated as

$$t_{\mathrm{n}j} = \begin{cases} z_{\mathrm{n}j} + \epsilon_{\mathrm{n}}\, \tilde{g}_j & \text{if} \quad z_{\mathrm{n}j} + \epsilon_{\mathrm{n}}\, \tilde{g}_j \le 0 \quad \text{(contact)} \\ 0 & \text{else} \quad \text{(no contact)} \ . \end{cases} \tag{46}$$

Similarly to the penalty regularized form (38), we introduce the tangential traction rate measure as

$$\mathcal{L}_v(\boldsymbol{t}_{\tau j} - \boldsymbol{z}_{\tau j}) = \epsilon_\tau \left[\tilde{\boldsymbol{v}}_{\tau j} - \beta \frac{\boldsymbol{t}_{\tau j}}{\|\boldsymbol{t}_{\tau j}\|} \right] \ , \tag{47}$$

together with (23a), (23c) and (23d).

The discrete force residual (18) is solved in a nested iterative scheme. The initial guess for the Lagrange multipliers is set, and the augmented iteration count ℓ is initialized

$$z^{(\ell)}_{\mathrm{n}j,n+1} = z_{\mathrm{n}j,n} \qquad \boldsymbol{z}^{(\ell)}_{\tau j,n+1} = \boldsymbol{z}_{\tau j,n} \qquad \ell = 0 \ . \tag{48}$$

Given the slip increment from time step n to $n+1$, the gap and the ℓth iterate for normal and tangential Lagrange multipliers: Compute a trial state, assuming no slip during the increment:

$$\begin{aligned} t^{(\ell)}_{\mathrm{n}j,n+1} &= z^{(\ell)}_{\mathrm{n}j,n+1} + \epsilon_{\mathrm{n}}\, \tilde{g}^{(\ell)}_{j,n+1} \\ \boldsymbol{t}^{\mathrm{trial},(\ell)}_{\tau j,n+1} &= \boldsymbol{z}^{(\ell)}_{\tau j,n+1} + \epsilon_\tau\, \boldsymbol{\tau}^{(\ell)}_{j,n+1}\, \tilde{\boldsymbol{u}}^{(\ell)}_{\tau j,n+1} \\ \varphi^{\mathrm{trial},(\ell)}_{j,n+1} &= \|\boldsymbol{t}^{\mathrm{trial},(\ell)}_{\tau j,n+1}\| - \mu\, t^{(\ell)}_{\mathrm{n}j,n+1} \end{aligned} \tag{49}$$

Determine contact status and update the tangential tractions $\boldsymbol{t}_{\tau j,n+1}$ using

$$\boldsymbol{t}^{(\ell)}_{\tau j,n+1} = \begin{cases} \boldsymbol{t}^{\mathrm{stick},(\ell)}_{\tau j,n+1} = \boldsymbol{t}^{\mathrm{trial},(\ell)}_{\tau j,n+1} & \text{if } \varphi^{\mathrm{trial},(\ell)}_{j,n+1} \le 0 \quad \text{(stick)} \\ \boldsymbol{t}^{\mathrm{slip},(\ell)}_{\tau j,n+1} = \boldsymbol{t}^{\mathrm{trial},(\ell)}_{\tau j,n+1} \frac{\mu\, t^{(\ell)}_{\mathrm{n}j,n+1}}{\|\boldsymbol{t}^{\mathrm{trial},(\ell)}_{\tau j,n+1}\|} & \text{else} \quad \text{(slip)} \ . \end{cases} \tag{50}$$

Update the normal and tangential nodal Lagrange multipliers using

$$z^{(\ell)}_{\mathrm{n}j,n+1} = t^{(\ell)}_{\mathrm{n}j,n+1} \qquad \text{and} \qquad \boldsymbol{z}^{(\ell)}_{\tau j,n+1} = \boldsymbol{t}^{(\ell)}_{\tau j,n+1} \ . \tag{51}$$

Assemble the global Lagrange multiplier vector

$$\boldsymbol{z}_{n+1}^{(\ell)} = \bigwedge_{j\in\mathcal{S}} z_{\mathrm{n}j,n+1}^{(\ell)}\, \boldsymbol{n}_{j,n+1}^{(\ell)} + \boldsymbol{z}_{\tau j,n+1}^{(\ell)} \quad . \tag{52}$$

Calculate the contact force using the two global mortar coupling matrices as in (17). Afterward, the discrete force residual (18) is solved for the displacements, while keeping the Lagrange multipliers constant. Finally, increase the iteration counter $\ell \leftarrow \ell + 1$. Repeat the loop, (49) through (52), until the contact constraints (21) and (23) are below some error norm $\varepsilon_{\mathrm{ALM}}$.

3. Adjoint based path-dependent sensitivity analysis

For transient systems, two competing variants of the adjoint method exist [1]. In the "time-continous" or "differentiate-then-discretize" variant, discretized primary and continuous time variables are used in the formulation of the adjoint problem. The solution is obtained by subsequently discretizing in time. In the "time-discrete" or "discretize-then-differentiate" variant, primary and time variables are discretized prior to the adjoint problem formulation. The "time-continous" approach is more commonly employed, as it is relatively simple in formulation and implementation as it is not tied to a specific time integration scheme. However, it may lead to inconsistent sensitivities [1]. The "time-discrete" variant is more complex to implement, but ensures that consistent sensitivities are found [1]. As sensitivity information is crucial to gradient based optimization algorithms, we choose the "time-discrete" variant of the adjoint method to derive consistent sensitivities.

We briefly repeat the sensitivity analysis with the "time-discrete" adjoint method for a general path-dependent system, following [31,32]. Assume that the problem depends on a set of design parameters $\boldsymbol{\phi} \in \mathbb{R}^{n_{\mathrm{design}}}$, e.g. representing the design densities in density based topology optimization. We rewrite the system (27) at pseudo time step n as functions of the design parameters $\boldsymbol{\phi}$ and the primary variables, $\boldsymbol{d}$ and $\boldsymbol{z}$,

$$\boldsymbol{R}_n\big(\boldsymbol{\phi}, \boldsymbol{d}_n(\boldsymbol{\phi}), \boldsymbol{d}_{n-1}(\boldsymbol{\phi}), \boldsymbol{z}_n(\boldsymbol{\phi}), \boldsymbol{z}_{n-1}(\boldsymbol{\phi})\big) = \boldsymbol{0} \quad , \tag{53a}$$

$$\boldsymbol{H}_n\big(\boldsymbol{\phi}, \boldsymbol{d}_n(\boldsymbol{\phi}), \boldsymbol{d}_{n-1}(\boldsymbol{\phi}), \boldsymbol{z}_n(\boldsymbol{\phi}), \boldsymbol{z}_{n-1}(\boldsymbol{\phi})\big) = \boldsymbol{0} \quad . \tag{53b}$$

Consider an objective function $\theta\big(\boldsymbol{\phi}, \boldsymbol{d}_1(\boldsymbol{\phi}), \dots, \boldsymbol{d}_N(\boldsymbol{\phi}), \boldsymbol{z}_1(\boldsymbol{\phi}), \dots, \boldsymbol{z}_N(\boldsymbol{\phi})\big)$ and its corresponding Lagrangian $\hat{\theta}$

$$\hat{\theta} = \theta + \sum_{n=1}^{N} \lambda_n^T\, \boldsymbol{R}_n + \sum_{n=1}^{N} \boldsymbol{\mu}_n^T\, \boldsymbol{H}_n \quad , \tag{54}$$

with $\lambda_n \in \mathbb{R}^{n_{\mathrm{dof}}}$ and $\boldsymbol{\mu}_n \in \mathbb{R}^{3n_{\mathrm{sl}}}$ the Lagrange multipliers associated with the displacement and contact residuals, (53a) and (53b). Note that $\hat{\theta} = \theta$ as $\boldsymbol{R}_n = \boldsymbol{0}$ (53a) and $\boldsymbol{H}_n = \boldsymbol{0}$ (53b). The linearization of the Lagrangian with respect to the design variables reads

$$\frac{\mathrm{d}\hat{\theta}}{\mathrm{d}\boldsymbol{\phi}} = \frac{\mathrm{d}\theta}{\mathrm{d}\boldsymbol{\phi}} + \sum_{n=1}^{N} \underbrace{\frac{\mathrm{d}\lambda_n^T}{\mathrm{d}\boldsymbol{\phi}}\, \boldsymbol{R}_n}_{\times} + \underbrace{\lambda_n^T \frac{\mathrm{d}\boldsymbol{R}_n}{\mathrm{d}\boldsymbol{\phi}}}_{\blacktriangle} + \sum_{n=1}^{N} \underbrace{\frac{\mathrm{d}\boldsymbol{\mu}_n^T}{\mathrm{d}\boldsymbol{\phi}}\, \boldsymbol{H}_n}_{\times} + \underbrace{\boldsymbol{\mu}_n^T \frac{\mathrm{d}\boldsymbol{H}_n}{\mathrm{d}\boldsymbol{\phi}}}_{\blacktriangle} \quad , \tag{55}$$

where the terms marked with an $\times$ vanish since $\boldsymbol{R}_n = \boldsymbol{0}$ and $\boldsymbol{H}_n = \boldsymbol{0}$. The terms marked with a $\blacktriangle$ vanish as well as $\mathrm{d}\boldsymbol{R}_n/\mathrm{d}\boldsymbol{\phi} = \boldsymbol{0}$ and $\mathrm{d}\boldsymbol{H}_n/\mathrm{d}\boldsymbol{\phi} = \boldsymbol{0}$, see [31] for details. Therefore, $\mathrm{d}\hat{\theta}/\mathrm{d}\boldsymbol{\phi} = \mathrm{d}\theta/\mathrm{d}\boldsymbol{\phi}$. To formulate the adjoint system the terms marked with a $\blacktriangle$ are kept, from (55) follows

$$\begin{aligned}
\frac{\mathrm{d}\hat{\theta}}{\mathrm{d}\boldsymbol{\phi}} = \frac{\mathrm{d}\theta}{\mathrm{d}\boldsymbol{\phi}} = \frac{\partial\theta}{\partial\boldsymbol{\phi}} &+ \sum_{n=1}^{N} \left(\frac{\partial\theta}{\partial\boldsymbol{d}_n} \frac{\mathrm{d}\boldsymbol{d}_n}{\mathrm{d}\boldsymbol{\phi}} + \frac{\partial\theta}{\partial\boldsymbol{z}_n} \frac{\mathrm{d}\boldsymbol{z}_n}{\mathrm{d}\boldsymbol{\phi}} \right) \\
&+ \sum_{n=1}^{N} \lambda_n^T \left(\frac{\partial\boldsymbol{R}_n}{\partial\boldsymbol{\phi}} + \frac{\partial\boldsymbol{R}_n}{\partial\boldsymbol{d}_n} \frac{\mathrm{d}\boldsymbol{d}_n}{\mathrm{d}\boldsymbol{\phi}} + \underbrace{\frac{\partial\boldsymbol{R}_n}{\partial\boldsymbol{d}_{n-1}} \frac{\mathrm{d}\boldsymbol{d}_{n-1}}{\mathrm{d}\boldsymbol{\phi}}}_{\star} + \frac{\partial\boldsymbol{R}_n}{\partial\boldsymbol{z}_n} \frac{\mathrm{d}\boldsymbol{z}_n}{\mathrm{d}\boldsymbol{\phi}} + \frac{\partial\boldsymbol{R}_n}{\partial\boldsymbol{z}_{n-1}} \frac{\mathrm{d}\boldsymbol{z}_{n-1}}{\mathrm{d}\boldsymbol{\phi}} \right) \\
&+ \sum_{n=1}^{N} \boldsymbol{\mu}_n^T \left(\frac{\partial\boldsymbol{H}_n}{\partial\boldsymbol{\phi}} + \frac{\partial\boldsymbol{H}_n}{\partial\boldsymbol{d}_n} \frac{\mathrm{d}\boldsymbol{d}_n}{\mathrm{d}\boldsymbol{\phi}} + \frac{\partial\boldsymbol{H}_n}{\partial\boldsymbol{d}_{n-1}} \frac{\mathrm{d}\boldsymbol{d}_{n-1}}{\mathrm{d}\boldsymbol{\phi}} + \frac{\partial\boldsymbol{H}_n}{\partial\boldsymbol{z}_n} \frac{\mathrm{d}\boldsymbol{z}_n}{\mathrm{d}\boldsymbol{\phi}} + \frac{\partial\boldsymbol{H}_n}{\partial\boldsymbol{z}_{n-1}} \frac{\mathrm{d}\boldsymbol{z}_{n-1}}{\mathrm{d}\boldsymbol{\phi}} \right) \quad .
\end{aligned} \tag{56}$$

In our setting the values $\boldsymbol{d}_0$ and $\boldsymbol{z}_0$ are fixed initial conditions, independent of $\boldsymbol{\phi}$. Note that this is not true in general [31]. The term marked with a $\star$ in (56) can be rewritten as

$$\sum_{n=1}^{N} \lambda_n^T \frac{\partial\boldsymbol{R}_n}{\partial\boldsymbol{d}_{n-1}} \frac{\mathrm{d}\boldsymbol{d}_{n-1}}{\mathrm{d}\boldsymbol{\phi}} = \sum_{m=0}^{N-1} \lambda_{m+1}^T \frac{\partial\boldsymbol{R}_{m+1}}{\partial\boldsymbol{d}_m} \frac{\mathrm{d}\boldsymbol{d}_m}{\mathrm{d}\boldsymbol{\phi}} = \lambda_1^T \frac{\partial\boldsymbol{R}_1}{\partial\boldsymbol{d}_0} \underbrace{\frac{\mathrm{d}\boldsymbol{d}_0}{\mathrm{d}\boldsymbol{\phi}}}_{=\boldsymbol{0}} + \sum_{m=1}^{N-1} \lambda_{m+1}^T \frac{\partial\boldsymbol{R}_{m+1}}{\partial\boldsymbol{d}_m} \frac{\mathrm{d}\boldsymbol{d}_m}{\mathrm{d}\boldsymbol{\phi}} \quad , \tag{57}$$

where the pseudo time step variable $m = 1, \dots, N-1$ is introduced. The same logic applies to all other derivatives with respect to previous time steps. Recombination of terms leads to

$$\begin{aligned}\frac{\mathrm{d}\hat{\theta}}{\mathrm{d}\boldsymbol{\phi}} = &\left[\frac{\partial\theta}{\partial\boldsymbol{\phi}} + \sum_{n=1}^{N}\left(\lambda_n^T\frac{\partial\boldsymbol{R}_n}{\partial\boldsymbol{\phi}} + \boldsymbol{\mu}_n^T\frac{\partial\boldsymbol{H}_n}{\partial\boldsymbol{\phi}}\right)\right] \\ &+ \left(\frac{\partial\theta}{\partial\boldsymbol{d}_N} + \lambda_N^T\frac{\partial\boldsymbol{R}_N}{\partial\boldsymbol{d}_N} + \boldsymbol{\mu}_N^T\frac{\partial\boldsymbol{H}_N}{\partial\boldsymbol{d}_N}\right)\frac{\mathrm{d}\boldsymbol{d}_N}{\mathrm{d}\boldsymbol{\phi}} + \sum_{m=1}^{N-1}\left(\frac{\partial\theta}{\partial\boldsymbol{d}_m} + \lambda_{m+1}^T\frac{\partial\boldsymbol{R}_{m+1}}{\partial\boldsymbol{d}_m} + \boldsymbol{\mu}_{m+1}^T\frac{\partial\boldsymbol{H}_{m+1}}{\partial\boldsymbol{d}_m} + \lambda_m^T\frac{\partial\boldsymbol{R}_m}{\partial\boldsymbol{d}_m} + \boldsymbol{\mu}_m^T\frac{\partial\boldsymbol{H}_m}{\partial\boldsymbol{d}_m}\right)\frac{\mathrm{d}\boldsymbol{d}_m}{\mathrm{d}\boldsymbol{\phi}} \\ &+ \left(\frac{\partial\theta}{\partial\boldsymbol{z}_N} + \lambda_N^T\frac{\partial\boldsymbol{R}_N}{\partial\boldsymbol{z}_N} + \boldsymbol{\mu}_N^T\frac{\partial\boldsymbol{H}_N}{\partial\boldsymbol{z}_N}\right)\frac{\mathrm{d}\boldsymbol{z}_N}{\mathrm{d}\boldsymbol{\phi}} + \sum_{m=1}^{N-1}\left(\frac{\partial\theta}{\partial\boldsymbol{z}_m} + \lambda_{m+1}^T\frac{\partial\boldsymbol{R}_{m+1}}{\partial\boldsymbol{z}_m} + \boldsymbol{\mu}_{m+1}^T\frac{\partial\boldsymbol{H}_{m+1}}{\partial\boldsymbol{z}_m} + \lambda_m^T\frac{\partial\boldsymbol{R}_m}{\partial\boldsymbol{z}_m} + \boldsymbol{\mu}_m^T\frac{\partial\boldsymbol{H}_m}{\partial\boldsymbol{z}_m}\right)\frac{\mathrm{d}\boldsymbol{z}_m}{\mathrm{d}\boldsymbol{\phi}} \quad . \end{aligned} \tag{58}$$

In order to avoid calculating the implicit derivatives $\mathrm{d}\boldsymbol{d}_n/\mathrm{d}\boldsymbol{\phi}$ and $\mathrm{d}\boldsymbol{z}_n/\mathrm{d}\boldsymbol{\phi}$, $n = 1, \dots, N$, Lagrange multipliers λ_n and $\boldsymbol{\mu}_n$ are chosen such that they are solutions to the adjoint system of equations

$$\begin{aligned} N\text{th step}: &\begin{cases} \dfrac{\partial\theta}{\partial\boldsymbol{d}_N} + \lambda_N^T\dfrac{\partial\boldsymbol{R}_N}{\partial\boldsymbol{d}_N} + \boldsymbol{\mu}_N^T\dfrac{\partial\boldsymbol{H}_N}{\partial\boldsymbol{d}_N} = \boldsymbol{0} \\ \dfrac{\partial\theta}{\partial\boldsymbol{z}_N} + \lambda_N^T\dfrac{\partial\boldsymbol{R}_N}{\partial\boldsymbol{z}_N} + \boldsymbol{\mu}_N^T\dfrac{\partial\boldsymbol{H}_N}{\partial\boldsymbol{z}_N} = \boldsymbol{0} \end{cases}, \\ m\text{th step}: &\begin{cases} \dfrac{\partial\theta}{\partial\boldsymbol{d}_m} + \lambda_{m+1}^T\dfrac{\partial\boldsymbol{R}_{m+1}}{\partial\boldsymbol{d}_m} + \boldsymbol{\mu}_{m+1}^T\dfrac{\partial\boldsymbol{H}_{m+1}}{\partial\boldsymbol{d}_m} + \lambda_m^T\dfrac{\partial\boldsymbol{R}_m}{\partial\boldsymbol{d}_m} + \boldsymbol{\mu}_m^T\dfrac{\partial\boldsymbol{H}_m}{\partial\boldsymbol{d}_m} = \boldsymbol{0} \\ \dfrac{\partial\theta}{\partial\boldsymbol{z}_m} + \lambda_{m+1}^T\dfrac{\partial\boldsymbol{R}_{m+1}}{\partial\boldsymbol{z}_m} + \boldsymbol{\mu}_{m+1}^T\dfrac{\partial\boldsymbol{H}_{m+1}}{\partial\boldsymbol{z}_m} + \lambda_m^T\dfrac{\partial\boldsymbol{R}_m}{\partial\boldsymbol{z}_m} + \boldsymbol{\mu}_m^T\dfrac{\partial\boldsymbol{H}_m}{\partial\boldsymbol{z}_m} = \boldsymbol{0} \end{cases} \qquad m = N-1, \dots, 1 \quad . \end{aligned} \tag{59}$$

The adjoint system of equations (59) are solved in opposing order to the forward problem at hand, i.e., starting at step N and ending at step 1. Rewriting (59) in matrix-vector form yields

$$\begin{aligned} N\text{th step}: &\begin{bmatrix} \frac{\partial\boldsymbol{R}_N}{\partial\boldsymbol{d}_N}^T & \frac{\partial\boldsymbol{H}_N}{\partial\boldsymbol{d}_N}^T \\ \frac{\partial\boldsymbol{R}_N}{\partial\boldsymbol{z}_N}^T & \frac{\partial\boldsymbol{H}_N}{\partial\boldsymbol{z}_N}^T \end{bmatrix}\begin{bmatrix} \lambda_N \\ \boldsymbol{\mu}_N \end{bmatrix} = -\begin{bmatrix} \frac{\partial\theta}{\partial\boldsymbol{d}_N}^T \\ \frac{\partial\theta}{\partial\boldsymbol{z}_N}^T \end{bmatrix}, \\ m\text{th step}: &\begin{bmatrix} \frac{\partial\boldsymbol{R}_m}{\partial\boldsymbol{d}_m}^T & \frac{\partial\boldsymbol{H}_m}{\partial\boldsymbol{d}_m}^T \\ \frac{\partial\boldsymbol{R}_m}{\partial\boldsymbol{z}_m}^T & \frac{\partial\boldsymbol{H}_m}{\partial\boldsymbol{z}_m}^T \end{bmatrix}\begin{bmatrix} \lambda_m \\ \boldsymbol{\mu}_m \end{bmatrix} = -\begin{bmatrix} \frac{\partial\theta}{\partial\boldsymbol{d}_m}^T \\ \frac{\partial\theta}{\partial\boldsymbol{z}_m}^T \end{bmatrix} - \begin{bmatrix} \frac{\partial\boldsymbol{R}_{m+1}}{\partial\boldsymbol{d}_m}^T & \frac{\partial\boldsymbol{H}_{m+1}}{\partial\boldsymbol{d}_m}^T \\ \frac{\partial\boldsymbol{R}_{m+1}}{\partial\boldsymbol{z}_m}^T & \frac{\partial\boldsymbol{H}_{m+1}}{\partial\boldsymbol{z}_m}^T \end{bmatrix}\begin{bmatrix} \lambda_{m+1} \\ \boldsymbol{\mu}_{m+1} \end{bmatrix} \qquad m = N-1, \dots, 1 \quad . \end{aligned} \tag{60}$$

On the left-hand sides of the adjoint systems we identify the transposed system matrix from the forward problem (36), which can be very conveniently reused here, if stored in the forward solve. The linearizations of the residuals $\boldsymbol{R}$ and $\boldsymbol{H}$ with respect to the primary variables at the current step, i.e.

$$\frac{\partial\boldsymbol{R}_n}{\partial\boldsymbol{d}_n}, \frac{\partial\boldsymbol{R}_n}{\partial\boldsymbol{z}_n}, \frac{\partial\boldsymbol{H}_n}{\partial\boldsymbol{d}_n} \text{ and } \frac{\partial\boldsymbol{H}_n}{\partial\boldsymbol{z}_n} \qquad n = 1, \dots, N \quad ,$$

are identical to the ones from the forward analysis, we refer to [21,23] for details. On the right-hand sides of the adjoint systems, there are the linearizations of the objective function with respect to the primary variables at the current step m and an additional term, the linearization of the residuals at step $m+1$ with respect to the primary variables at step m, i.e.

$$\frac{\partial\boldsymbol{R}_{m+1}}{\partial\boldsymbol{d}_m}, \frac{\partial\boldsymbol{R}_{m+1}}{\partial\boldsymbol{z}_m}, \frac{\partial\boldsymbol{H}_{m+1}}{\partial\boldsymbol{d}_m} \text{ and } \frac{\partial\boldsymbol{H}_{m+1}}{\partial\boldsymbol{z}_m} \qquad m = N-1, \dots, 1 \quad .$$

They depend on the type of constraint enforcement strategy (LMM, PM, ALM) and are discussed in the following in Sections 3.1, 3.2 and 3.3. After the solution of the adjoint systems for λ_n and $\boldsymbol{\mu}_n$, the sensitivity is obtained from (58) as

$$\frac{\mathrm{d}\theta}{\mathrm{d}\boldsymbol{\phi}} = \frac{\mathrm{d}\hat{\theta}}{\mathrm{d}\boldsymbol{\phi}} = \frac{\partial\theta}{\partial\boldsymbol{\phi}} + \sum_{n=1}^{N}\left(\lambda_n^T\frac{\partial\boldsymbol{R}_n}{\partial\boldsymbol{\phi}} + \boldsymbol{\mu}_n^T\frac{\partial\boldsymbol{H}_n}{\partial\boldsymbol{\phi}}\right) \quad . \tag{61}$$

Exemplary linearizations that are related to the objective function θ and/or the design parameters $\boldsymbol{\phi}$,

$$\frac{\partial\theta}{\partial\boldsymbol{\phi}}, \frac{\partial\theta}{\partial\boldsymbol{d}_n}, \frac{\partial\theta}{\partial\boldsymbol{z}_n}, \frac{\partial\boldsymbol{R}_n}{\partial\boldsymbol{\phi}} \text{ and } \frac{\partial\boldsymbol{H}_n}{\partial\boldsymbol{\phi}},$$

are discussed in Sections 4.1 and 4.2.

3.1. Lagrange multiplier method

For elastic materials the linearizations of the residual $\boldsymbol{R}$ with respect to the previous time step variables are

$$\frac{\partial\boldsymbol{R}_{m+1}}{\partial\boldsymbol{d}_m} = \frac{\partial\boldsymbol{f}_{\mathrm{int},m+1} + \boldsymbol{f}_{\mathrm{co},m+1} - \boldsymbol{f}_{\mathrm{ext},m+1}}{\partial\boldsymbol{d}_m} = \boldsymbol{0} \qquad \text{and} \qquad \frac{\partial\boldsymbol{R}_{m+1}}{\partial\boldsymbol{z}_m} = \frac{\partial\boldsymbol{f}_{\mathrm{int},m+1} + \boldsymbol{f}_{\mathrm{co},m+1} - \boldsymbol{f}_{\mathrm{ext},m+1}}{\partial\boldsymbol{z}_m} = \boldsymbol{0} \quad . \tag{62}$$

For the contact residual $\boldsymbol{H}$ (35), we derive the linearization of the normal and tangential complementarity functions utilizing the active/inactive and stick/slip separation from the forward problem solution. The linearizations of the normal nonlinear complementarity function for inactive (31) and active (32) nodes with respect to the previous time step are

$$\frac{\partial C_{\mathrm{n}j,\mathcal{I},m+1}}{\partial \boldsymbol{d}_m} = \frac{\partial z_{\mathrm{n}j,m+1}}{\partial \boldsymbol{d}_m} = \boldsymbol{0} \qquad \text{and} \qquad \frac{\partial C_{\mathrm{n}j,\mathcal{A},m+1}}{\partial \boldsymbol{d}_m} = \frac{\partial c_{\mathrm{n}}\, \tilde{g}_{j,m+1}}{\partial \boldsymbol{d}_m} = \boldsymbol{0} \ . \tag{63}$$

The linearization of the tangential complementarity function for stick nodes (33) is

$$\frac{\partial \boldsymbol{C}_{\tau j,St,m+1}}{\partial \boldsymbol{d}_m} = -\mu\,(z_{\mathrm{n}j,m+1} - c_{\mathrm{n}}\tilde{g}_{j,m+1})c_\tau \frac{\partial \tilde{\boldsymbol{u}}_{\tau j,m+1}}{\partial \boldsymbol{d}_m} \ , \tag{64}$$

for slip nodes (34) it is

$$\frac{\partial \boldsymbol{C}_{\tau j,Sl,m+1}}{\partial \boldsymbol{d}_m} = \frac{\boldsymbol{z}_{\tau j,m+1} + c_\tau \tilde{\boldsymbol{u}}_{\tau j,m+1}}{\|\boldsymbol{z}_{\tau j,m+1} + c_\tau \tilde{\boldsymbol{u}}_{\tau j,m+1}\|} c_\tau \frac{\partial \tilde{\boldsymbol{u}}_{\tau j,m+1}}{\partial \boldsymbol{d}_m} \boldsymbol{z}_{\tau j,m+1} - \mu\,(z_{\mathrm{n}j,m+1} - c_{\mathrm{n}}\tilde{g}_{j,m+1})c_\tau \frac{\partial \tilde{\boldsymbol{u}}_{\tau j,m+1}}{\partial \boldsymbol{d}_m} \ , \tag{65}$$

with the linearization of the nodal slip increment (24) with respect to the previous time step

$$\frac{\partial \tilde{\boldsymbol{u}}_{\tau j,m+1}}{\partial \boldsymbol{d}_m} = \boldsymbol{\tau}^T_{j,m+1} \frac{\partial \mathbf{D}[j,j]_m}{\partial \boldsymbol{d}_m} \boldsymbol{x}^{(1)}_{j,m+1} - \boldsymbol{\tau}^T_{j,m+1} \sum_{l=1}^{n_m} \frac{\partial \mathbf{M}[j,l]_m}{\partial \boldsymbol{d}_m} \boldsymbol{x}^{(2)}_{l,m+1} \ . \tag{66}$$

For the linearization of the mortar sub-matrices $\mathbf{D}[j,j]$ and $\mathbf{M}[j,l]$ we refer to [21]. As the contact residual $\boldsymbol{H}$ does not depend on the previous time step contact Lagrange multipliers, its linearization is

$$\frac{\partial \boldsymbol{H}_{m+1}}{\partial \boldsymbol{z}_m} = \boldsymbol{0} \ . \tag{67}$$

3.2. Penalty method

As the penalty regularized discrete force residual (44) is formulated in displacement variables only, the adjoint framework simplifies considerably. The Lagrangian is

$$\hat{\theta} = \theta + \sum_{n=1}^{N} \lambda_n^T \boldsymbol{R}_n \ . \tag{68}$$

Following the outline above, the adjoint system of equations is

$$\begin{aligned} N\text{th step} &: \frac{\partial \boldsymbol{R}_N}{\partial \boldsymbol{d}_N}^T \lambda_N = -\frac{\partial \theta}{\partial \boldsymbol{d}_N}^T \ , \\ m\text{th step} &: \frac{\partial \boldsymbol{R}_m}{\partial \boldsymbol{d}_m}^T \lambda_m = -\frac{\partial \theta}{\partial \boldsymbol{d}_m}^T - \frac{\partial \boldsymbol{R}_{m+1}}{\partial \boldsymbol{d}_m}^T \lambda_{m+1} \qquad m = N-1,\dots,1 \ . \end{aligned} \tag{69}$$

The sensitivity is obtained as

$$\frac{\mathrm{d}\theta}{\mathrm{d}\boldsymbol{\phi}} = \frac{\mathrm{d}\hat{\theta}}{\mathrm{d}\boldsymbol{\phi}} = \frac{\partial \theta}{\partial \boldsymbol{\phi}} + \sum_{n=1}^{N} \lambda_n^T \frac{\partial \boldsymbol{R}_n}{\partial \boldsymbol{\phi}} \ . \tag{70}$$

For penalty regularization, the linearization of the discrete force residual (44) does not vanish. It reads

$$\frac{\partial \boldsymbol{R}_{m+1}}{\partial \boldsymbol{d}_m} = \frac{\partial \boldsymbol{f}_{\mathrm{int},m+1} + \boldsymbol{f}_{\mathrm{co},m+1} - \boldsymbol{f}_{\mathrm{ext},m+1}}{\partial \boldsymbol{d}_m} = \frac{\partial \boldsymbol{f}_{\mathrm{co},m+1}}{\partial \boldsymbol{d}_m} = \begin{bmatrix} \boldsymbol{0} & -\boldsymbol{M}_{m+1} & \boldsymbol{D}_{m+1} \end{bmatrix}^T \frac{\partial \boldsymbol{t}_{m+1}}{\partial \boldsymbol{d}_m} \ , \tag{71}$$

wherein

$$\frac{\partial \boldsymbol{t}_{m+1}}{\partial \boldsymbol{d}_m} = \mathop{\mathbf{A}}_{j\in S} \underbrace{\frac{\partial t_{\mathrm{n}j,m+1}\, \boldsymbol{n}_{j,m+1}}{\partial \boldsymbol{d}_m}}_{=\boldsymbol{0}} + \frac{\partial \boldsymbol{t}_{\tau j,m+1}}{\partial \boldsymbol{d}_m} = \mathop{\mathbf{A}}_{j\in S} \frac{\partial \boldsymbol{t}_{\tau j,m+1}}{\partial \boldsymbol{d}_m} \ . \tag{72}$$

Depending on a node's stick/slip state in the forward problem at step $m+1$, either the stick or slip traction has to be linearized. The linearization of the nodal tangential stick traction is

$$\frac{\partial \boldsymbol{t}^{\mathrm{stick}}_{\tau j,m+1}}{\partial \boldsymbol{d}_m} = \frac{\partial \boldsymbol{t}^{\mathrm{trial}}_{\tau j,m+1}}{\partial \boldsymbol{d}_m} \ , \tag{73}$$

$$\frac{\partial \boldsymbol{t}^{\mathrm{trial}}_{\tau j,m+1}}{\partial \boldsymbol{d}_m} = \frac{\partial \boldsymbol{t}_{\tau j,m} + \epsilon_\tau\, \boldsymbol{\tau}_{j,m+1}\, \tilde{\boldsymbol{u}}_{\tau j,m+1}}{\partial \boldsymbol{d}_m} = \frac{\partial \boldsymbol{t}_{\tau j,m}}{\partial \boldsymbol{d}_m} + \epsilon_\tau\, \boldsymbol{\tau}_{j,m+1} \frac{\partial \tilde{\boldsymbol{u}}_{\tau j,m+1}}{\partial \boldsymbol{d}_m} \ , \tag{74}$$

where $\partial \boldsymbol{t}_{\tau j,m}/\partial \boldsymbol{d}_m$ depends on the node's stick/slip state at step m and can be re-used from the forward solve, and the linearization of the nodal slip increment (66). Linearization of the nodal tangential slip traction is

$$\begin{aligned}\frac{\partial \boldsymbol{t}^{\text{slip}}_{\tau j,m+1}}{\partial \boldsymbol{d}_m} &= \frac{\partial}{\partial \boldsymbol{d}_m}\left(\boldsymbol{t}^{\text{trial}}_{\tau j,m+1}\frac{\mu\, t_{\text{n}j,m+1}}{\|\boldsymbol{t}^{\text{trial}}_{\tau j,m+1}\|}\right)\\ &= \frac{\partial \boldsymbol{t}^{\text{trial}}_{\tau j,m+1}}{\partial \boldsymbol{d}_m}\frac{\mu\, t_{\text{n}j,m+1}}{\|\boldsymbol{t}^{\text{trial}}_{\tau j,m+1}\|} + \boldsymbol{t}^{\text{trial}}_{\tau j,m+1}\underbrace{\frac{\partial \mu\, t_{\text{n}j,m+1}}{\partial \boldsymbol{d}_m}}_{=\boldsymbol{0}}\frac{1}{\|\boldsymbol{t}^{\text{trial}}_{\tau j,m+1}\|} + \boldsymbol{t}^{\text{trial}}_{\tau j,m+1}\,\mu\, t_{\text{n}j,m+1}\frac{\partial \|\boldsymbol{t}^{\text{trial}}_{\tau j,m+1}\|}{\partial \boldsymbol{d}_m}\frac{-1}{\left(\|\boldsymbol{t}^{\text{trial}}_{\tau j,m+1}\|\right)^2}\,.\end{aligned} \tag{75}$$

Using

$$\frac{\partial \|\boldsymbol{t}^{\text{trial}}_{\tau j,m+1}\|}{\partial \boldsymbol{d}_m} = \frac{\boldsymbol{t}^{\text{trial}}_{\tau j,m+1}}{\|\boldsymbol{t}^{\text{trial}}_{\tau j,m+1}\|}\frac{\partial \boldsymbol{t}^{\text{trial}}_{\tau j,m+1}}{\partial \boldsymbol{d}_m}\,, \tag{76}$$

this can be rewritten as

$$\frac{\partial \boldsymbol{t}^{\text{slip}}_{\tau j,m+1}}{\partial \boldsymbol{d}_m} = \frac{\partial \boldsymbol{t}^{\text{trial}}_{\tau j,m+1}}{\partial \boldsymbol{d}_m}\frac{\mu\, t_{\text{n}j,m+1}}{\|\boldsymbol{t}^{\text{trial}}_{\tau j,m+1}\|} - \frac{\partial \boldsymbol{t}^{\text{trial}}_{\tau j,m+1}}{\partial \boldsymbol{d}_m}\left(\boldsymbol{t}^{\text{trial}}_{\tau j,m+1}\right)^2\frac{\mu\, t_{\text{n}j,m+1}}{\left(\|\boldsymbol{t}^{\text{trial}}_{\tau j,m+1}\|\right)^3}\,, \tag{77}$$

with the linearization of the trial traction (74).

3.3. Augmented Lagrangian method

In the forward problem, we utilized an Uzawa type algorithm in combination with the ALM to determine the contact Lagrange multipliers, see Section 2.5. The scheme iterates until the nodal contact constraints (21) and (23) are satisfied up to a certain tolerance. We can reformulate the nodal contact constraints using the nonlinear complementarity functions as we did for the LMM, see Section 2.3.1, and formulate the contact residual $\boldsymbol{H}$ (35) as in Section 2.3.2. Therefore, we have two systems of equations, the discrete force residual $\boldsymbol{R}$ (18) and the contact residual $\boldsymbol{H}$ (35), as in the LMM, see Section 2.3. We use both residuals to construct the Lagrangian (54), see Section 3. This enables us to follow the same path-dependent adjoint approach as we did for the LMM, solving a saddle-point system in each adjoint step.

We linearize the state from the ALM iteration, where the nodal contact constraints are satisfied. For readability, we drop the superscript (ℓ). To construct this saddle-point system, four matrix blocks are required at each time step. The linearization of the discrete force residual (18) with respect to the displacement field, $\partial \boldsymbol{R}_n/\partial \boldsymbol{d}_n$, can be reused from the forward system solve, for details on the linearization see [16]. The blocks $\partial \boldsymbol{R}_n/\partial \boldsymbol{z}_n$, $\partial \boldsymbol{H}_n/\partial \boldsymbol{d}_n$ and $\partial \boldsymbol{H}_n/\partial \boldsymbol{z}_n$ are the same as for the LMM, see [23].

Similar as in the PM, see (71), the linearization of the discrete force residual (18) with respect to the previous time step does not vanish. It is

$$\frac{\partial \boldsymbol{R}_{m+1}}{\partial \boldsymbol{d}_m} = \frac{\partial \boldsymbol{f}_{\text{int},m+1} + \boldsymbol{f}_{\text{co},m+1} - \boldsymbol{f}_{\text{ext},m+1}}{\partial \boldsymbol{d}_m} = \frac{\partial \boldsymbol{f}_{\text{co},m+1}}{\partial \boldsymbol{d}_m} = \begin{bmatrix}\boldsymbol{0} & -\boldsymbol{M}_{m+1} & \boldsymbol{D}_{m+1}\end{bmatrix}^T\frac{\partial \boldsymbol{z}_{m+1}}{\partial \boldsymbol{d}_m}\,, \tag{78}$$

wherein the linearization of the assembled Lagrange multiplier vector is

$$\frac{\partial \boldsymbol{z}_{m+1}}{\partial \boldsymbol{d}_m} = \underbrace{\mathop{\mathsf{A}}_{j\in\mathcal{S}}\frac{\partial z_{\text{n}j,m+1}\,\boldsymbol{n}_{m+1}}{\partial \boldsymbol{d}_m}}_{=\boldsymbol{0}} + \frac{\partial \boldsymbol{z}_{\tau j,m+1}}{\partial \boldsymbol{d}_m} = \mathop{\mathsf{A}}_{j\in\mathcal{S}}\frac{\partial \boldsymbol{z}_{\tau j,m+1}}{\partial \boldsymbol{d}_m}\,. \tag{79}$$

The linearization of the tangential nodal Lagrange multipliers depends on the nodes' stick/slip state in the forward problem. If node j is in stick state in step $m+1$

$$\frac{\partial \boldsymbol{z}_{\tau j,m+1}}{\partial \boldsymbol{d}_m} = \frac{\partial \boldsymbol{t}^{\text{stick}}_{\tau j,m+1}}{\partial \boldsymbol{d}_m} = \frac{\partial \boldsymbol{t}^{\text{trial}}_{\tau j,m+1}}{\partial \boldsymbol{d}_m}\,, \tag{80}$$

with the linearization of the trial traction

$$\frac{\partial \boldsymbol{t}^{\text{trial}}_{\tau j,m+1}}{\partial \boldsymbol{d}_m} = \frac{\partial \boldsymbol{z}_{\tau j,m+1}}{\partial \boldsymbol{d}_m} + \frac{\partial \epsilon_\tau\,\boldsymbol{\tau}_{j,m+1}\,\tilde{\boldsymbol{u}}_{\tau j,m+1}}{\partial \boldsymbol{d}_m} = \epsilon_\tau\,\boldsymbol{\tau}_{j,m+1}\frac{\partial \tilde{\boldsymbol{u}}_{\tau j,m+1}}{\partial \boldsymbol{d}_m}\,. \tag{81}$$

If node j is in slip state in step $m+1$

$$\begin{aligned}\frac{\partial \boldsymbol{z}_{\tau j,m+1}}{\partial \boldsymbol{d}_m} &= \frac{\partial \boldsymbol{t}^{\text{slip}}_{\tau j,m+1}}{\partial \boldsymbol{d}_m} = \frac{\partial}{\partial \boldsymbol{d}_m}\left(\boldsymbol{t}^{\text{trial}}_{\tau j,m+1}\frac{\mu\, t_{\text{n}j,m+1}}{\|\boldsymbol{t}^{\text{trial}}_{\tau j,m+1}\|}\right)\\ &= \frac{\partial \boldsymbol{t}^{\text{trial}}_{\tau j,m+1}}{\partial \boldsymbol{d}_m}\frac{\mu\, t_{\text{n}j,m+1}}{\|\boldsymbol{t}^{\text{trial}}_{\tau j,m+1}\|} + \boldsymbol{t}^{\text{trial}}_{\tau j,m+1}\underbrace{\frac{\partial \mu\, t_{\text{n}j,m+1}}{\partial \boldsymbol{d}_m}}_{=\boldsymbol{0}}\frac{1}{\|\boldsymbol{t}^{\text{trial}}_{\tau j,m+1}\|} + \boldsymbol{t}^{\text{trial}}_{\tau j,m+1}\,\mu\, t_{\text{n}j,m+1}\frac{\partial \|\boldsymbol{t}^{\text{trial}}_{\tau j,m+1}\|}{\partial \boldsymbol{d}_m}\frac{-1}{\left(\|\boldsymbol{t}^{\text{trial}}_{\tau j,m+1}\|\right)^2}\,.\end{aligned} \tag{82}$$

Using

$$\frac{\partial \|\boldsymbol{t}^{\text{trial}}_{\tau j,m+1}\|}{\partial \boldsymbol{d}_m} = \frac{\boldsymbol{t}^{\text{trial}}_{\tau j,m+1}}{\|\boldsymbol{t}^{\text{trial}}_{\tau j,m+1}\|} \frac{\partial \boldsymbol{t}^{\text{trial}}_{\tau j,m+1}}{\partial \boldsymbol{d}_m} \quad , \tag{83}$$

this can be rewritten as

$$\frac{\partial \boldsymbol{z}_{\tau j,m+1}}{\partial \boldsymbol{d}_m} = \frac{\partial \boldsymbol{t}^{\text{trial}}_{\tau j,m+1}}{\partial \boldsymbol{d}_m} \frac{\mu\, t_{\text{n}j,m+1}}{\|\boldsymbol{t}^{\text{trial}}_{\tau j,m+1}\|} - \frac{\partial \boldsymbol{t}^{\text{trial}}_{\tau j,m+1}}{\partial \boldsymbol{d}_m} \left(\boldsymbol{t}^{\text{trial}}_{\tau j,m+1}\right)^2 \frac{\mu\, t_{\text{n}j,m+1}}{\left(\|\boldsymbol{t}^{\text{trial}}_{\tau j,m+1}\|\right)^3} \quad , \tag{84}$$

with the linearization of the trial traction (81). The discrete force residual (18) does not explicitly depend on the previous time step Lagrange multipliers, its linearization is

$$\frac{\partial \boldsymbol{R}_{m+1}}{\partial \boldsymbol{z}_m} = \boldsymbol{0} \quad . \tag{85}$$

As the contact residual $\boldsymbol{H}$ (35) is the same as in the LMM, the linearizations are derived accordingly as presented in Section 3.1 in (63) through (67).

4. Optimization formulation

4.1. Density based topology optimization

For the design parametrization we use the standard density method, with one element-wise constant volume fraction $\phi^{(e)} \in [0,1]$ for each finite element in the design domain $\Omega_{\text{design}} \subseteq \Omega$. We apply the modified Solid Isotropic Material with Penalization (SIMP) [33]

$$E^{(e)} = \left[\phi_{\min} + (1-\phi_{\min})\phi^{(e)p}\right] E_0 \quad , \tag{86}$$

where $\phi_{\min}$ is a lower bound on the design parameters, p the penalization power and E_0 the Young's modulus of the solid material. For details on density based topology optimization we refer to [34]. To avoid numerical instabilities such as checkerboard patterns, a sensitivity filter with filter radius r_{filter} as presented in [35,36] is utilized.

The constrained optimization problem to minimize a generic objective function θ is formulated as

$$\begin{aligned} &\min_{\boldsymbol{\phi}} : \theta(\boldsymbol{\phi}) \\ &\text{subject to} : V(\boldsymbol{\phi}) \leq V_{\max} \\ &\qquad\quad : \boldsymbol{0} \leq \boldsymbol{\phi} \leq \boldsymbol{1} \quad , \end{aligned} \tag{87}$$

where $V(\boldsymbol{\phi}) = \sum_{(e)\in\Omega_{\text{design}}} \phi^{(e)} v^{(e)} / V_{\text{design}}$ is the filled volume fraction in the design domain with $v^{(e)}$ the volume of the e-th element, V_{design} the volume of the design domain and $V_{\max}$ an upper limit.

We can now derive the linearization of the residuals with respect to the design parameters. For each pseudo time step n the linearization of the discrete force residual (18) with respect to the design parameters is

$$\frac{\partial \boldsymbol{R}_n}{\partial \boldsymbol{\phi}} = \frac{\partial \boldsymbol{f}_{\text{int},n}}{\partial \boldsymbol{\phi}} + \frac{\partial \boldsymbol{f}_{\text{co},n}}{\partial \boldsymbol{\phi}} - \frac{\partial \boldsymbol{f}_{\text{ext},n}}{\partial \boldsymbol{\phi}} = \frac{\partial \boldsymbol{f}_{\text{int},n}}{\partial \boldsymbol{\phi}} \quad , \tag{88}$$

where the partial derivatives for the contact and the external forces vanish as those contributions do not depend on the design parameters explicitly. The linearization of the internal force vector with respect to the design parameters is

$$\frac{\partial \boldsymbol{f}_{\text{int},n}}{\partial \boldsymbol{\phi}} = \mathop{\mathsf{A}}_{e\in\Omega_{\text{design}}} \frac{\partial \boldsymbol{f}^{(e)}_{\text{int},n}}{\partial \boldsymbol{\phi}} = \mathop{\mathsf{A}}_{e\in\Omega_{\text{design}}} \frac{\partial \left[\phi_{\min} + (1-\phi_{\min})\phi^{(e)p}\right] \boldsymbol{f}^{(e)}_{\text{int},n,E_0}}{\partial \boldsymbol{\phi}} = \mathop{\mathsf{A}}_{e\in\Omega_{\text{design}}} (1-\phi_{\min})\, p\, (\phi^{(e)})^{p-1}\, \boldsymbol{f}^{(e)}_{\text{int},n,E_0} \quad . \tag{89}$$

For consistent linearization it is necessary to evaluate the element internal force vector $\boldsymbol{f}^{(e)}_{\text{int},n}$ with $E^{(e)} = E_0$ and apply the linearized modified SIMP scaling afterward. An "E_0" subscript is added to indicate this. Note, this does not restrict the design densities at the contact interfaces to solid. The linearization of the contact residual (35) with respect to the design parameters is

$$\frac{\partial \boldsymbol{H}_n}{\partial \boldsymbol{\phi}} = \boldsymbol{0} \quad . \tag{90}$$

4.2. Objective functions

Remaining, not yet discussed linearizations $\partial\theta/\partial\boldsymbol{\phi}$, $\partial\theta/\partial\boldsymbol{d}_n$ and $\partial\theta/\partial\boldsymbol{z}_n$ depend on the respective choice of the objective function. The two objective functions discussed in the following measure the force at the contact interface at one specific time step (91) and summed over all time steps (96). To generate stiff structures, the idea is to maximize the force norm measure. This is achieved by minimizing the negative force norm measure. Other choices are of course possible.

4.2.1. Force magnitude

We define the objective function $\theta_{\text{force},s}$, evaluated at a single pseudo time step $s \in [1, N]$, as

$$\theta_{\text{force},s}(\boldsymbol{\phi}, \boldsymbol{d}_s(\boldsymbol{\phi})) = -\sum_{j \in S} \| \boldsymbol{f}_{\text{int},s}^{(j)} \| \quad , \tag{91}$$

where we introduced the nodal internal force vector $\boldsymbol{f}_{\text{int},s}^{(j)} \in \mathbb{R}^3$ which is a subset of the internal force vector $\boldsymbol{f}_{\text{int},s}$. S is the set containing all slave side contact nodes. Note, the internal force vector $\boldsymbol{f}_{\text{int},s}$ does not contain the contact force vector $\boldsymbol{f}_{\text{co},s}$, see (18). The linearization with respect to the design parameters is

$$\frac{\partial \theta_{\text{force},s}}{\partial \boldsymbol{\phi}} = \frac{\partial \theta_{\text{force},s}}{\partial \boldsymbol{f}_{\text{int},s}} \frac{\partial \boldsymbol{f}_{\text{int},s}}{\partial \boldsymbol{\phi}} \quad , \tag{92}$$

where the linearization of the internal force vector with respect to the design parameters is given in (89). The linearization of the objective function with respect to the internal force vector is

$$\frac{\partial \theta_{\text{force},s}}{\partial \boldsymbol{f}_{\text{int},s}} = -\mathop{\mathbb{A}}_{j \in S} \frac{\boldsymbol{f}_{\text{int},s}^{(j)}}{\| \boldsymbol{f}_{\text{int},s}^{(j)} \|} \quad . \tag{93}$$

Similarly, we derive the linearization of the objective function with respect to the displacement field as

$$\frac{\partial \theta_{\text{force},s}}{\partial \boldsymbol{d}_n} = \begin{cases} \frac{\partial \theta_{\text{force},s}}{\partial \boldsymbol{f}_{\text{int},s}} \frac{\partial \boldsymbol{f}_{\text{int},s}}{\partial \boldsymbol{d}_s} & \text{if } s == n \quad , \\ \boldsymbol{0} & \text{else} \quad , \end{cases} \tag{94}$$

where the linearization of the internal force vector with respect to the displacement field follows standard finite element linearization. The linearization with respect to the contact Lagrange multipliers is

$$\frac{\partial \theta_{\text{force},s}}{\partial \boldsymbol{z}_n} = \boldsymbol{0} \quad . \tag{95}$$

4.2.2. Sum of force magnitude

We define the objective function $\theta_{\text{force,all}}$ as sum of the objective function $\theta_{\text{force},s}$ over all steps $s = 1, \dots, N$

$$\theta_{\text{force,all}}(\boldsymbol{\phi}, \boldsymbol{d}_n(\boldsymbol{\phi})) = \sum_{s=1}^{N} \theta_{\text{force},s} = -\sum_{s=1}^{N} \sum_{j \in S} \| \boldsymbol{f}_{\text{int},s}^{(j)} \| \quad . \tag{96}$$

The linearization with respect to the design parameters is

$$\frac{\partial \theta_{\text{force,all}}}{\partial \boldsymbol{\phi}} = \sum_{s=1}^{N} \frac{\partial \theta_{\text{force},s}}{\partial \boldsymbol{f}_{\text{int},s}} \frac{\partial \boldsymbol{f}_{\text{int},s}}{\partial \boldsymbol{\phi}} \quad , \tag{97}$$

where the linearization of the internal force vector with respect to the design parameters is given in (89). The linearization of the objective function $\theta_{\text{force},s}$ with respect to the internal forces is given in (93). Similarly, the linearization of the objective function $\theta_{\text{force,all}}$ with respect to the displacement field for all steps n is

$$\frac{\partial \theta_{\text{force,all}}}{\partial \boldsymbol{d}_n} = \frac{\partial \theta_{\text{force},n}}{\partial \boldsymbol{f}_{\text{int},n}} \frac{\partial \boldsymbol{f}_{\text{int},n}}{\partial \boldsymbol{d}_n} \quad . \tag{98}$$

The linearization with respect to the contact Lagrange multipliers for all steps n is

$$\frac{\partial \theta_{\text{force,all}}}{\partial \boldsymbol{z}_n} = \boldsymbol{0} \quad . \tag{99}$$

5. Examples

In this section we present several topology optimization examples that utilize the methods introduced in this contribution. We demonstrate that the consideration of frictional contact constraints as compared with a frictionless assumption severely impacts the resulting optimized designs.

For simplicity, several parameters and properties are the same for all examples presented in this section, unless stated otherwise. Pseudo time runs from $t_0 = 0.0$ to $t_{\text{end}} = 1.0$. All bodies are meshed using first-order hexahedral finite elements. Standard shape functions are used for the interpolation of the nodal values of the Lagrange multiplier field. Dual shape functions could be employed correspondingly. A coupled form of the compressible neo-Hookean constitutive model [37]

$$\Psi_{\text{NH}}(I_1, J) = \frac{c}{\beta}\left(J^{-2\beta}\right) + c\left(I_1 - 3\right) \tag{100}$$

is used, with the first principal invariant $I_1 = \text{tr}(\boldsymbol{F}^T \boldsymbol{F})$, the Jacobian $J = \det(\boldsymbol{F})$, where $\boldsymbol{F} = \partial \boldsymbol{x}(\boldsymbol{X}, t)/\partial \boldsymbol{X}$ is the deformation gradient, and constants $c = \frac{E}{4(1+\nu)}$ and $\beta = \frac{\nu}{1-2\nu}$. The densities in the design domain Ω_{design} are initialized homogeneously as $\phi^{(e)} = \phi_{\text{init}}$. For

the design domain the modified SIMP interpolation scheme (86) with penalization power $p = 3$ is applied. In regularization strategies, i.e. in PM and ALM, we choose the same penalization parameter in normal and tangential direction $\epsilon = \epsilon_n = \epsilon_\tau$.

We will utilize the two objective functions introduced above, see (91) and (96). When used, we will evaluate the objective function $\theta_{\text{force},s}$ at step $s = N$, we denote this by $\theta_{\text{force},N}$. All the examples are Dirichlet constrained, the prescribed displacements are tabulated in the respective problem setups. In between the specified values, the displacements are linearly interpolated.

To solve the optimization problem, the gradient-based Method of Moving Asymptotes (MMA) [38], version 1.5 from 2007 is used, which can be obtained from [39]. The parameters are chosen as given in the accompanying notes [40], unless stated otherwise. For a more conservative optimizer the bound move limit was decreased to 0.1. The resolution of the optimized designs is direct result of the finite element discretization.

In each time step n of the forward problem, the nonlinear system of equations is solved iteratively with a fully linearized Newton-Raphson procedure until the absolute norm of the discrete force residual (18) is below ε_{res} and the absolute norm displacement increment $\Delta \boldsymbol{d}^k$ in (29) is below $\varepsilon_{\text{disp}}$. If contact is modeled using the LMM, the Newton loop additionally has to satisfy that the absolute norm of the contact residual (35) is below ε_{con} and the absolute norm of the Lagrange multiplier increment, $\Delta \boldsymbol{z}^k$ in (29), is below ε_{LMM}. If contact is modeled using the ALM, the Uzawa loop iterates until the contact constraints (21) and (23) satisfy ε_{ALM}.

The sensitivities derived using the path-dependent adjoint framework presented in this publication were checked with a finite difference scheme. They agree for all three contact enforcement methods.

5.1. Cube on cuboid

A cube consisting of one single finite element is pressed onto and moved over a cuboid consisting of four finite elements. The problem setup is presented in Fig. 2. We compare the sensitivities resulting from the three contact constraint enforcement strategies LMM, PM and ALM presented in this contribution. Forward and sensitivity analysis is performed for the initial design, the design parametrization is not optimized. The study is done with two distinct friction coefficients, such that at step N all contacting nodes are in stick ($\mu = 0.5$) or in slip ($\mu = 0.2$) state.

The problem is solved using $N = 10$ pseudo time steps. The material parameters for both bodies are $E_0 = 1000.0$ and $\nu = 0.3$. All elements are included in the design domain Ω_{design}. The initial design density is $\phi_{\text{init}} = 0.5$, the minimal density is $\phi_{\text{min}} = 0.0$. The error norms for displacement increment and residual are $\varepsilon_{\text{disp}} = 10^{-9}$ and $\varepsilon_{\text{res}} = 10^{-9}$. The compared contact formulations are the PM with different penalization parameters $\epsilon = \{100, 200, 500, 1000, 2000\}$, ALM with $\epsilon = 1000$ and KKT tolerance $\varepsilon_{\text{ALM}} = 10^{-6}$ and LMM with $\varepsilon_{\text{LMM}} = 10^{-6}$ and $\varepsilon_{\text{con}} = 10^{-6}$. As objective function the force norm at the last time step $\theta_{\text{force},N}$ (91) is minimized. The sensitivity filter is not applied.

For both tests similar behavior can be observed, see Fig. 3. We choose the LMM solution as our reference solution to compare to. Values obtained using the ALM are close, which can be expected as the ALM combined with an Uzawa type algorithm approximates the LMM. When using the PM, with increasing penalization parameters the values slowly converge towards the LMM results. High penalization parameters lead to an ill-conditioned system, in our case the forward problem aborted unsuccessful for $\epsilon > 2000$.

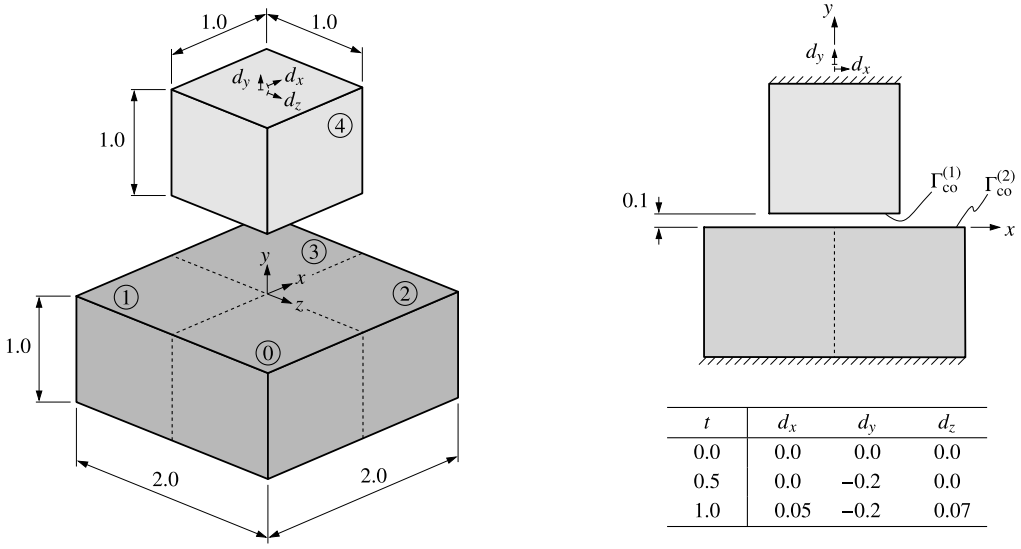

t	d_x	d_y	d_z
0.0	0.0	0.0	0.0
0.5	0.0	−0.2	0.0
1.0	0.05	−0.2	0.07

Fig. 2. Cube on cuboid problem setup. The numbers ⓪ to ④ label the elements and are referenced in Fig. 3. The right drawing visualizes the configuration at $t = 0.0$.

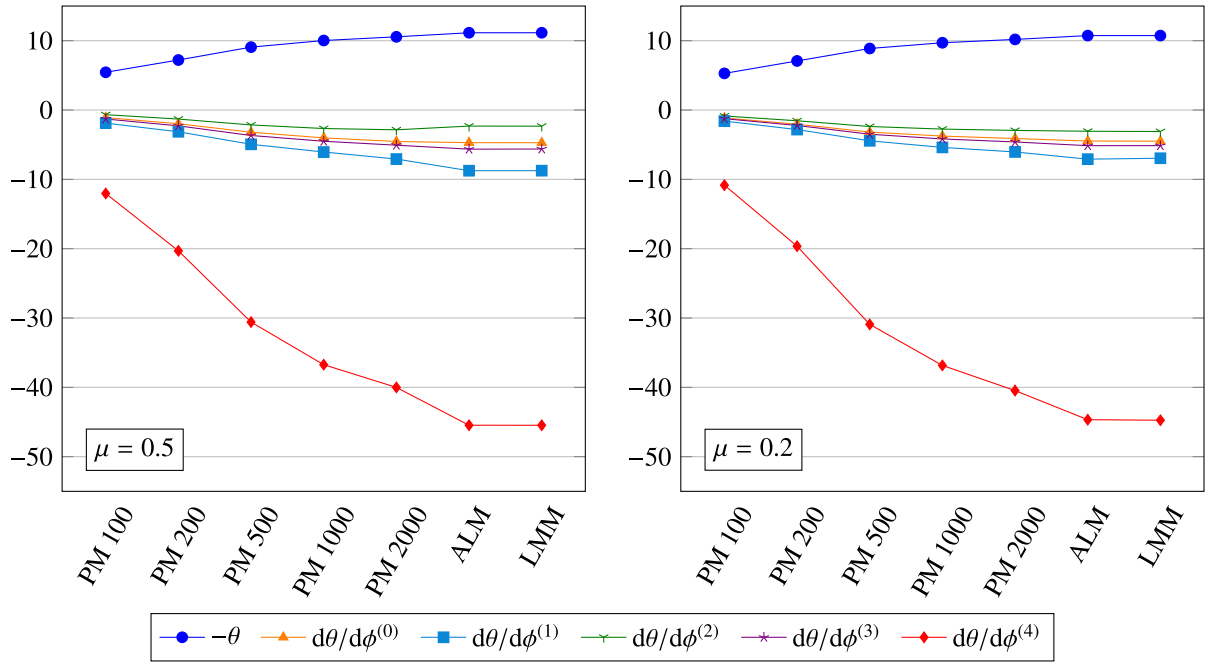

Fig. 3. Comparison of objective values and sensitivities using distinct contact regularizations for cube on cuboid problem. The friction coefficients are chosen such that at step N all contacting nodes are in stick ($\mu = 0.5$, left chart) or in slip ($\mu = 0.2$, right chart) state. PM X is the penalty method with $X = \epsilon_n = \epsilon_\tau$, ALM is the augmented Lagrangian method and LMM is the Lagrange multiplier method, according to Section 2.4, 2.5, and 2.3, respectively.

5.2. Half sphere on plate

In this example we first study the resulting designs for the introduced objective functions with various friction coefficients, see Section 5.2.1. Then we compare the resulting designs using the different constraint enforcement algorithms, see Section 5.2.2. The example setup, which is the same in both studies, is given in Fig. 4.

The example is solved using $N = 50$ time steps. The half sphere ($E_0 = 1000.0$, $\nu = 0.3$, 2808 finite elements) is not optimized, while the plate ($E_0 = 1000.0$, $\nu = 0.3$, 6561 finite elements) is the design domain with $\phi_{\text{init}} = 0.2$ and $\phi_{\min} = 10^{-3}$. A constraint on the volume fraction, $V_{\max} = 0.2$, is employed. Sensitivity filtering with $r_{\text{filter}} = 0.5$ is applied. The norms for displacement increment and residual are $\varepsilon_{\text{disp}} = 10^{-5}$ and $\varepsilon_{\text{res}} = 10^{-7}$. The MMA asymptote update parameters are chosen as $\alpha_{\text{init}} = 0.8$, $\alpha_{\text{incr}} = 1.2$ and $\alpha_{\text{decr}} = 0.65$.

5.2.1. Study on friction coefficient and objective functions

We compare the designs resulting from frictionless ($\mu = 0.0$) and frictional ($\mu = 0.3$) contact. Additionally, we compare the introduced objective functions $\theta_{\text{force,N}}$ and $\theta_{\text{force,all}}$, see Eqs. (91) and (96). Contact is modeled using the LMM with $\epsilon_{\text{LMM}} = 10^{-4}$ and $\epsilon_{\text{con}} = 10^{-4}$.

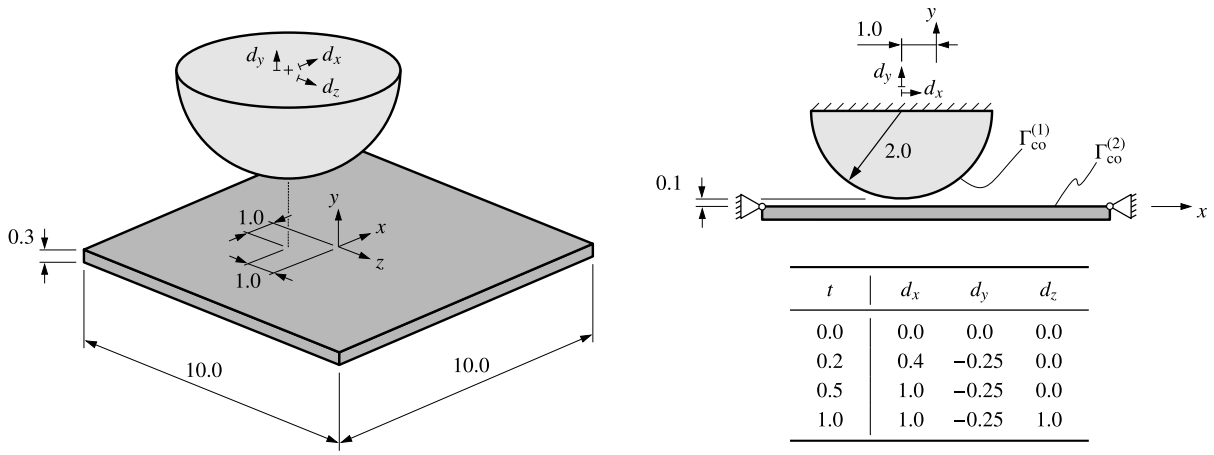

t	d_x	d_y	d_z
0.0	0.0	0.0	0.0
0.2	0.4	−0.25	0.0
0.5	1.0	−0.25	0.0
1.0	1.0	−0.25	1.0

Fig. 4. Half sphere on plate problem setup, configuration for $t = 0.0$ visualized.

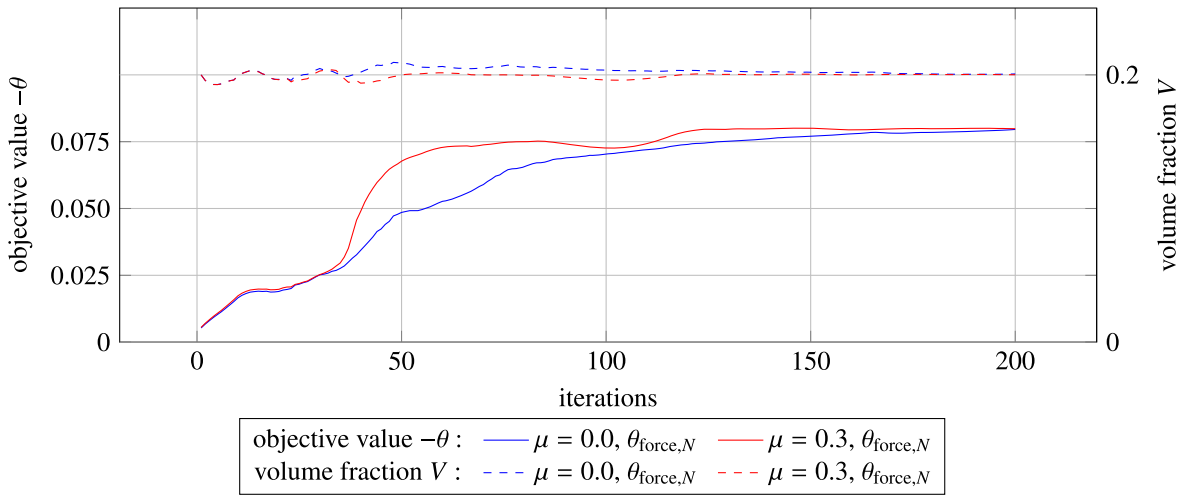

Fig. 5. Comparison of objective values for half sphere on plate problem for friction coefficients $\mu = \{0.0, 0.3\}$ and objective function $\theta_{\text{force,N}}$.

The evolution of the objective values and the volume fractions for the cases considering the $\theta_{\text{force,N}}$ objective function is depicted in Fig. 5. Fig. 6 depicts the evolution for the cases considering the $\theta_{\text{force,all}}$ objective function.

The optimized density distributions after 200 optimization iterations are depicted in Fig. 7.

In Fig. 7a a result with two symmetry axes in the xz-plane can be seen. When a frictionless setup ($\mu = 0.0$) is chosen and only the last time step is considered in the objective function ($\theta_{\text{force,N}}$), the load-path prior to the last time step is not considered in the objective evaluation and the sensitivity analysis and thus does not affect the result. This, together with the choice of prescribed displacement (starting off-center and ending at $x = 0.0$ and $z = 0.0$) leads to the depicted result symmetry.

Choosing a frictional setup ($\mu = 0.3$), the objective function ($\theta_{\text{force,N}}$) now depends on the full load-path, as can be seen in Fig. 7b. The resulting design now shows some directional dependence, which results from the prescribed displacement, see the table in the problem setup, Fig. 4.

When considering a frictionless setup and an objective function that includes the whole load-path ($\theta_{\text{force,all}}$), the final design reflects that choice, see Fig. 7c. In Fig. 7d the resulting design for a frictional setup with all time steps considered in the objective function ($\theta_{\text{force,all}}$) is depicted, which is the most path-dependent case of the four examples.

5.2.2. Study on contact enforcement methods

We optimize the objective function $\theta_{\text{force,N}}$, considering a friction coefficient of $\mu = 0.3$. The compared contact constraint enforcement approaches are the PM with penalization parameter $\epsilon = 1000$, the ALM with $\epsilon = 100$ and KKT tolerance $\varepsilon_{\text{ALM}} = 10^{-9}$ and the LMM with $\varepsilon_{\text{LMM}} = 10^{-4}$ and $\varepsilon_{\text{con}} = 10^{-4}$. The evolution of the objective values and the volume fractions for all contact enforcement methods is depicted in Fig. 8. Note that the curves for the ALM and the LMM are almost indistinguishable.

The optimized density distributions after 200 optimization iterations are depicted in Fig. 9.

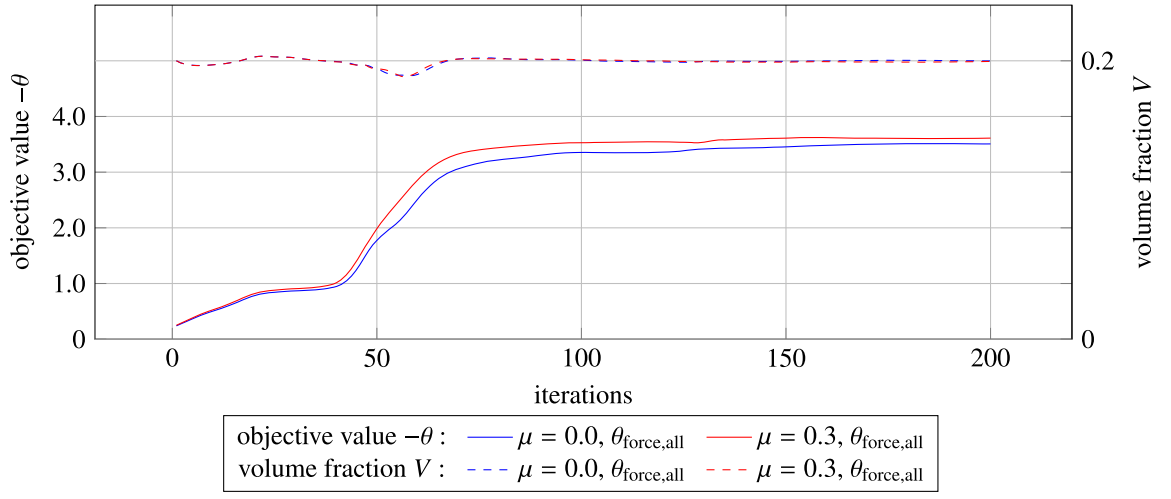

Fig. 6. Comparison of objective values for half sphere on plate problem for friction coefficients $\mu = \{0.0, 0.3\}$ and objective function $\theta_{\text{force,all}}$.

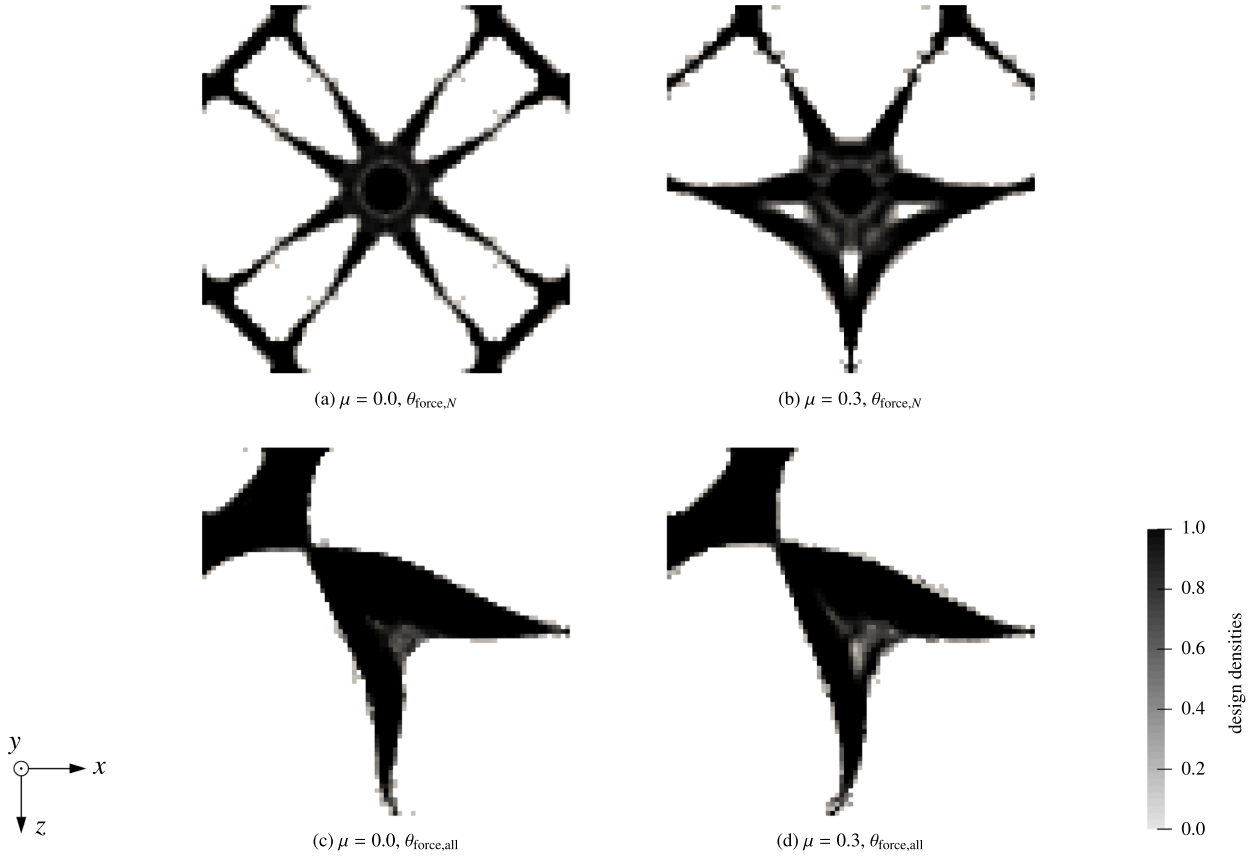

Fig. 7. Comparison of resulting designs for half sphere on plate problem for friction coefficients $\mu = \{0.0, 0.3\}$ and objective functions $\theta_{\text{force,N}}$ and $\theta_{\text{force,all}}$.

Although different constraint enforcement strategies were utilized, the resulting designs are quite close. The objective values for the resulting designs are $\theta^{\text{PM}}_{\text{force,N}} = 75.46 \cdot 10^{-3}$, $\theta^{\text{ALM}}_{\text{force,N}} = 79.60 \cdot 10^{-3}$ and $\theta^{\text{LMM}}_{\text{force,N}} = 79.86 \cdot 10^{-3}$. It is to be noted that the design for the penalty regularized case, see Fig. 9a, is dependent on the penalization parameter ϵ.

5.3. Ironing

The ironing problem is a well known example in contact mechanics [30,42], whereas several variants do exist [21,23]. In [2] it is topology optimized using frictionless contact mechanics. We compare the resulting designs for varying frictional coefficients, $\mu = \{0.0, 0.1, 0.25\}$. The problem setup is presented in Fig. 10.

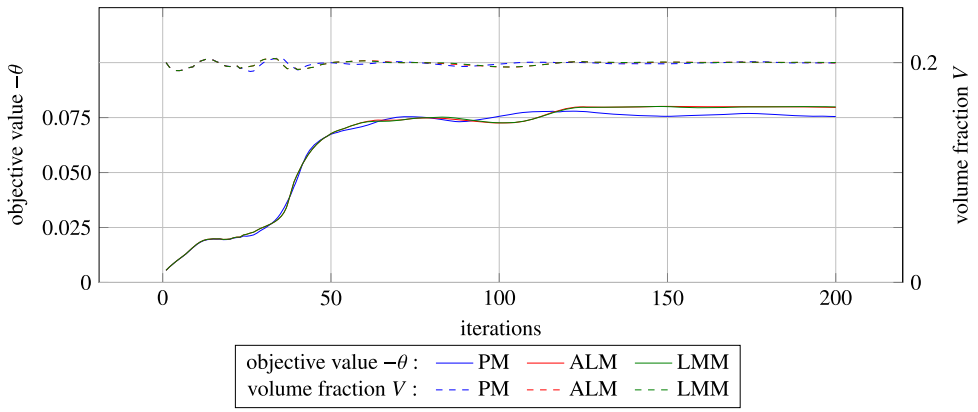

Fig. 8. Comparison of objective values for half sphere on plate problem for the different contact enforcement strategies using a friction coefficient $\mu = 0.3$ and objective function $\theta_{\text{force,N}}$.

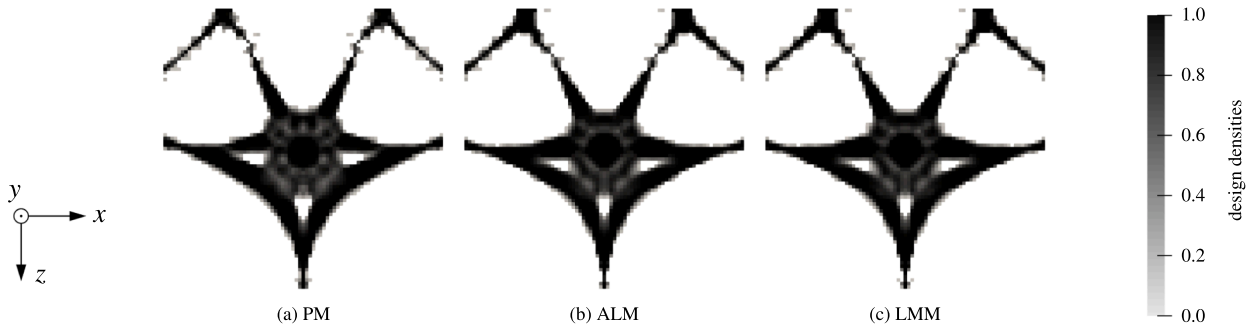

Fig. 9. Comparison of resulting designs for half sphere on plate problem with $\mu = 0.3$ and $\theta_{\text{force,N}}$ for the different contact enforcement methods.

The example is solved using $N = 200$ time steps. The semicircular die ($E_0 = 1000$, $\nu = 0.3$, 71 finite elements) is not optimized, while the block ($E_0 = 1$, $\nu = 0.3$, 4050 finite elements) is the design domain with $\phi_{\text{init}} = 0.4$ and $\phi_{\text{min}} = 10^{-3}$. As objective function the force norm summed over all time steps $\theta_{\text{force,all}}$ is minimized, see Eq. (96). A constraint on the volume fraction, $V_{\text{max}} = 0.4$, is employed. Sensitivity filtering with $r_{\text{filter}} = 0.5$ is applied.

The norms for displacement increment and residual are $\varepsilon_{\text{disp}} = 10^{-5}$ and $\varepsilon_{\text{res}} = 10^{-5}$. Contact is modeled using the LMM with $\varepsilon_{\text{LMM}} = 0.5 \cdot 10^{-4}$ and $\varepsilon_{\text{con}} = 10^{-7}$. The MMA asymptote update parameters are chosen as $\alpha_{\text{init}} = 0.5$, $\alpha_{\text{incr}} = 1.1$ and $\alpha_{\text{decr}} = 0.65$.

The evolution of the objective values and the volume fractions for all cases is depicted in Fig. 11. Comparing the curves for the objective values it can clearly be seen that the converged objective value increases with the friction coefficient.

The evolution of the objective function is typical for topology optimization that includes highly nonlinear mechanics, as the optimization problem is non-convex and shows various local minima. At approximately optimization iteration 190 the objective value and volume fraction drop significantly (but smoothly) within a few optimization iterations and recover in the following. The convergence behavior can be explained by the used optimization algorithm and the post-processing of the design sensitivities. First, we use a version of the MMA [39,40] that does not enforce a monotonic reduction of the objective, even if the constraints are satisfied. Second, we follow the established work of [35,36] and filter the sensitivities to avoid checker-boarding, promote smooth design, and reduce mesh dependence. The observed convergence of the optimization problem does not indicate inaccurate sensitivities, nor instabilities related to solving the forward problem.

In Fig. 12 the evolution of the deformations is shown for some exemplary time steps. The density distributions after 500 optimization iterations are depicted.

In Fig. 12a to 12c the design for the frictionless case is depicted. As the prescribed displacement is chosen to be symmetric with respect to the block yz-midplane at $x = 4.5$, a symmetric density distribution is expected. The wide support area on the contact slave surface results from the chosen objective function, $\theta_{\text{force,all}}$ (96).

Considering a frictional coefficient, $\mu = \{0.1, 0.25\}$, the resulting design reflects the path-dependence from the prescribed displacements, see Fig. 12d to 12f and 12g to 12i, respectively. As we maximize the force on the contact slave surface summed over all steps, see (96), the asymmetry increases with increasing friction coefficient.

Crosschecking of the optimized results has been performed. The results are listed in Table 1.

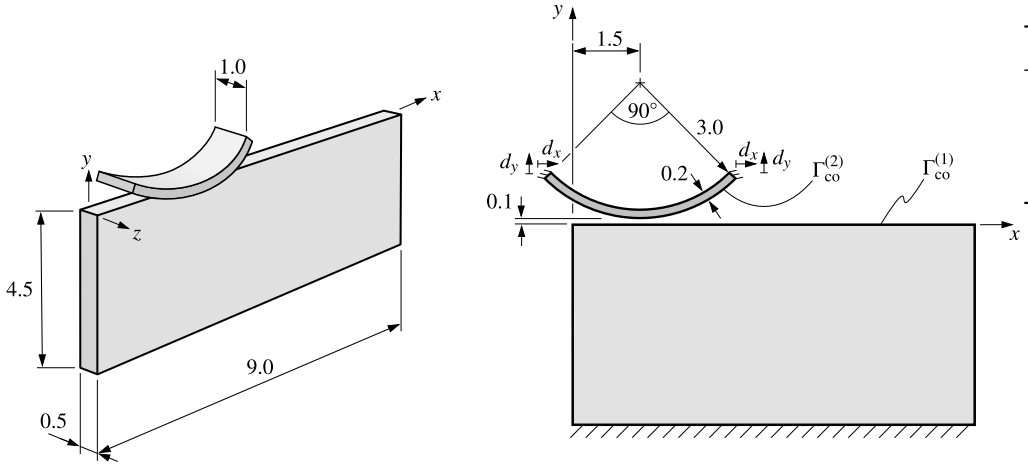

t	d_x	d_y
0.0	0.0	0.0
0.25	1.5	−0.2
0.75	4.5	−0.2
1.0	6.0	0.0

Fig. 10. Ironing problem setup, configuration for $t = 0.0$ visualized.

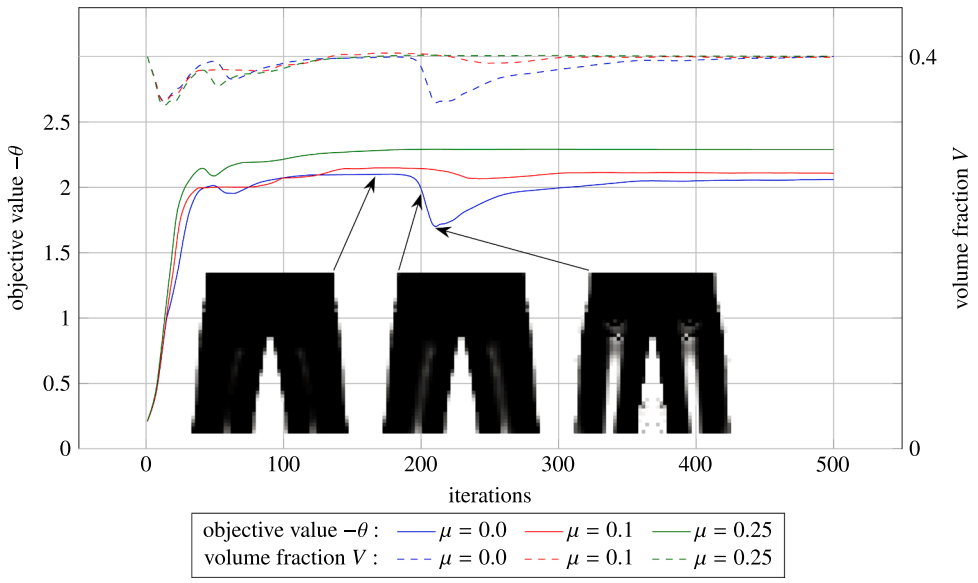

Fig. 11. Evolution of objective and volume fraction for different friction coefficients for ironing problem.

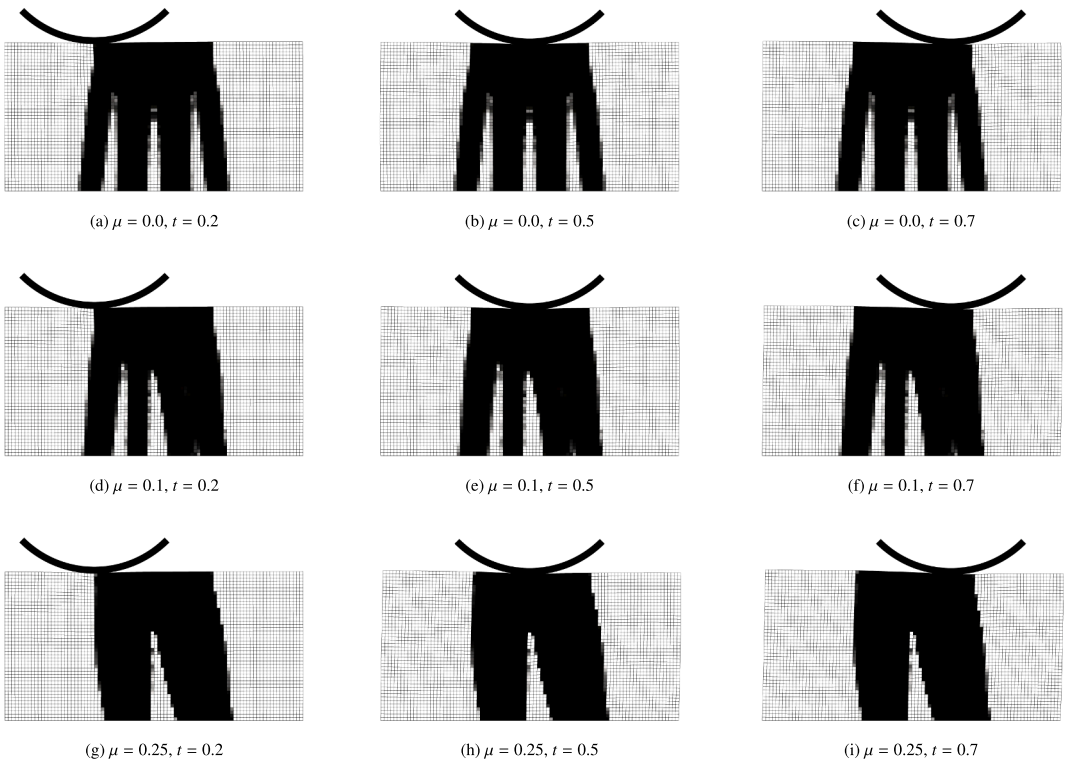

Fig. 12. Ironing problem deformed configurations for different time steps. Case with $\mu = 0.0$ is depicted in (a)-(c), $\mu = 0.25$ in (d)-(f) and $\mu = 0.25$ in (g)-(i).

By comparing the values in each row, one can see how the different designs perform for a given friction coefficient. The first row shows that the frictionless design and the design for a small friction coefficient ($\mu = 0.1$) perform similarly in a frictionless setup. The second row shows that the two designs optimized considering friction perform similarly for a friction coefficient of $\mu = 0.1$. As shown in the third row, the structure optimized for a frictionless setup ($\mu = 0.0$) performs 7.3 % worse than the structure optimized for an evaluation friction coefficient of $\mu = 0.25$. While the differences in the objective values are small at low friction coefficients, this study shows that variation in performance increases with the friction coefficient.

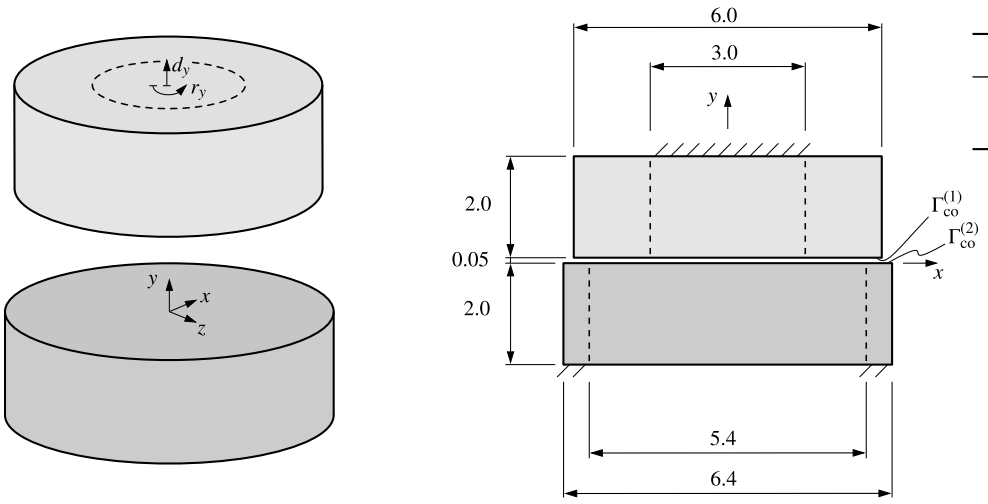

t	d_y	r_y
0.0	0.0	0°
1.0	−0.15	45°

Fig. 13. Clutch problem setup. Right drawing visualizes configuration for t = 0.0.

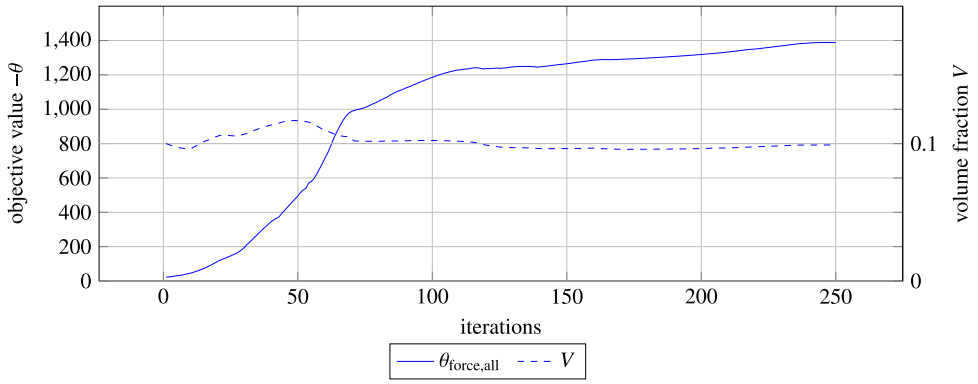

Fig. 14. Evolution of the objective value and volume fraction for the clutch problem.

5.4. Clutch

In the final example both bodies are part of the design domain. The problem setup is presented in Fig. 13.

The example is solved using $N = 100$ time steps. Both cylindric bodies ($E_0 = 1000$, $\nu = 0.3$, upper 46,848, lower 43,008 finite elements) are optimized, with $\phi_{\text{init}} = 0.2$ and $\phi_{\min} = 10^{-3}$. The friction coefficient is chosen to $\mu = 0.2$. As objective function the force norm summed over all time steps, $\theta_{\text{force,all}}$ (96), is minimized. A constraint on the volume fraction, $V_{\max} = 0.1$, is employed. Sensitivity filtering with $r_{\text{filter}} = 0.5$ is applied. The norms for displacement increment and residual are $\varepsilon_{\text{disp}} = 10^{-3}$ and $\varepsilon_{\text{res}} = 10^{-3}$. Contact is modeled using the ALM with $\epsilon = 100$ and $\varepsilon_{\text{ALM}} = 10^{-3}$. The MMA asymptote update parameters are chosen as $\alpha_{\text{init}} = 0.5$, $\alpha_{\text{incr}} = 1.05$ and $\alpha_{\text{decr}} = 0.5$.

The evolution of the objective value and the volume fraction is depicted in Fig. 14.

Table 1
Crosschecking for ironing problem. Each row lists the objective for the three different designs using one of the friction coefficients.

		optimization		
		$\mu = 0.0$	$\mu = 0.1$	$\mu = 0.25$
evaluation	$\mu = 0.0$	2.060	**2.063**	2.037
	$\mu = 0.1$	2.069	2.107	**2.109**
	$\mu = 0.25$	2.120	2.222	**2.287**
volume fraction		0.39996	0.39929	0.40027
evaluation normalized by volume fraction	$\mu = 0.0$	5.151	**5.166**	5.089
	$\mu = 0.1$	5.173	**5.276**	5.269
	$\mu = 0.25$	5.301	5.565	**5.714**

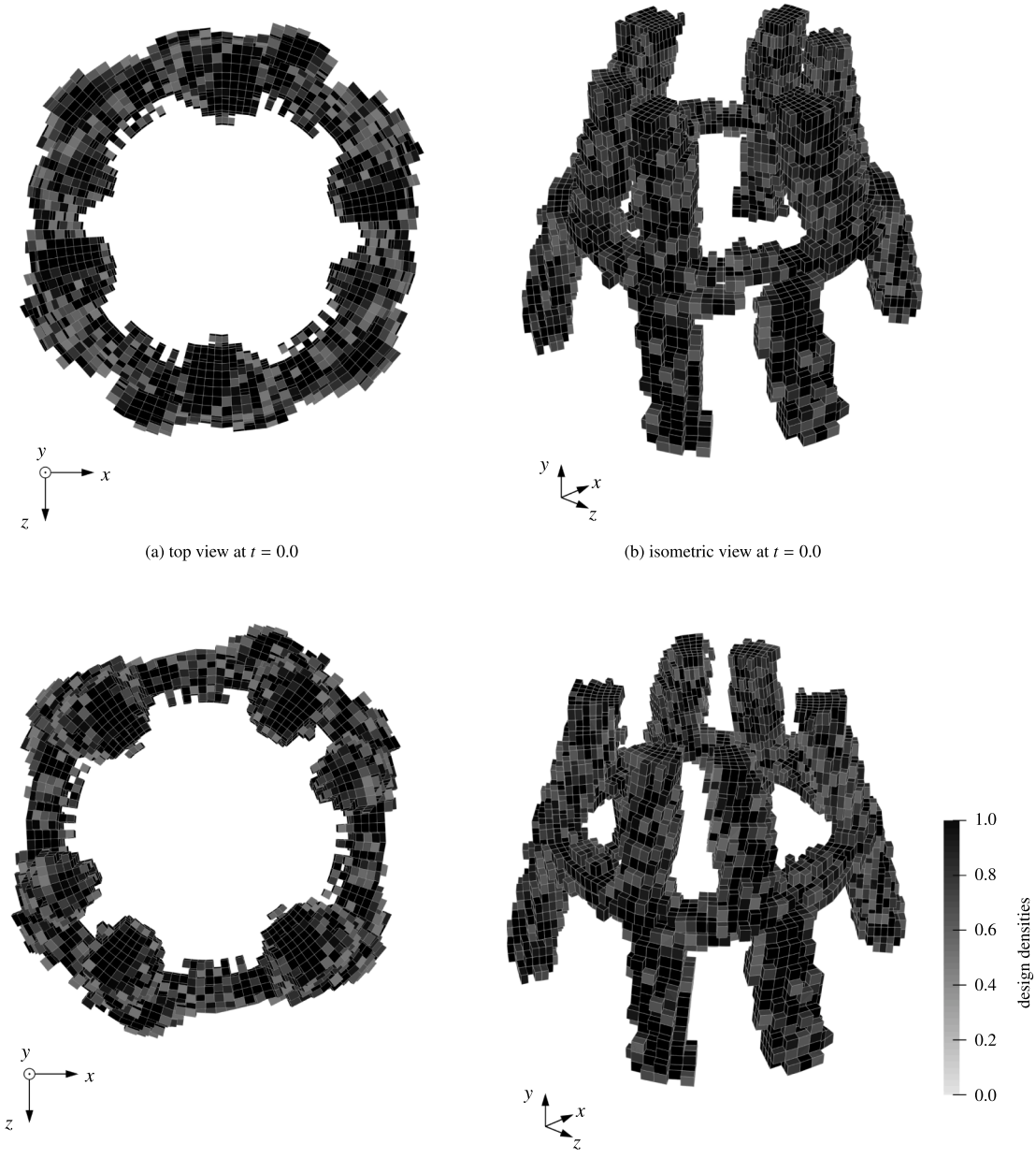

(a) top view at $t = 0.0$

(b) isometric view at $t = 0.0$

(c) top view at $t = 1.0$

(d) isometric view at $t = 1.0$

Fig. 15. Clutch example: Top (a) and (c) and isometric (b) and (d) views of the density distribution after 250 optimization iterations. The undeformed state ($t = 0.0$) is visualized in (a) and (b), the deformed state ($t = 1.0$) in (c) and (d). Only finite elements with design densities $\phi^{(e)} > 0.5$ are visualized.

The density distribution after 250 optimization iterations is depicted in Fig. 15, where the objective value reaches a plateau. The utilized finite element mesh has a two-fold symmetry in the xz-plane. This symmetry can be identified in the optimized design.

The upper cylinder compresses the lower one under rotation, see the table in Fig. 13. Maximal compression is reached at the final time step. Therefore, the last time step contributes the most to the objective function $\theta_{\text{force,all}}$. This explains why the vertical support structures of the upper and lower cylinder are optimized to align at the last time step shown, see Fig. 15d.

6. Discussion and conclusion

This contribution has presented a consistent sensitivity analysis framework for finite deformation problems involving frictional contact. A state-of-the-art mortar finite element approach has been employed for the spatial discretization of contact and frictional

sliding terms. Contact constraints have been enforced using three widely used methods: the Lagrange multiplier method (LMM), the augmented Lagrangian method (ALM), and the penalty method (PM). A density-based topology optimization problem has been formulated for the frictional contact setting. Since the resulting nonlinear optimization problem is solved iteratively, efficient sensitivity computation is essential. To this end, we have employed the adjoint method, which is well-suited for problems with a large number of design variables. The required full analytical linearizations have been derived and presented.

In the forward problem, contact constraints are reformulated using nonlinear complementarity functions, which enable the use of Newton-type algorithms not only for geometrical and material nonlinearities but also for nonlinearities arising from contact.

When constructing the Lagrangians for the LMM and ALM formulations, these complementarity functions, together with the discrete force residual, are incorporated, leading to a saddle-point system for the adjoint problem. As a result, the LMM requires solving saddle-point systems for both the forward and adjoint problems, which imposes specific requirements on the linear solver at each Newton iteration. A key advantage of the semi-smooth Newton method is the simultaneous solve for displacements and Lagrange multipliers. With the re-used tangent operator from the forward problem, each adjoint problem involves one linear system solve only.

In contrast, for the PM, both the forward and adjoint problems are formulated solely in terms of displacement variables, which offers advantages in the choice and efficiency of linear solvers. However, the PM only recovers the LMM solution in the limit as the penalty parameter $\epsilon \to \infty$, which is impractical due to the ill-conditioning of the system matrices at high penalty values.

In the ALM forward problem, the residual is linearized only with respect to displacement variables, resulting in a linear system similar to that in the PM. However, the ALM requires an additional iterative loop in the forward solve. In the adjoint problem, the ALM again leads to a saddle-point system, which does not require an iterative scheme but still necessitates an appropriate linear solver.

Independent of the contact enforcement method, each time step of the adjoint method only requires one linear system solve. Thus, the solution of the adjoint system is cheap compared to the forward system solve, especially for the ALM.

Due to the backward-in-time nature of the adjoint method in path-dependent problems, various quantities from the forward solve must be stored. At each time step, the transposed system matrices, as well as the transposed linearizations of the residuals with respect to the primary variables at the previous time step, are required. The latter depends, amongst others, on the linearization of the nodal slip increment with respect to the displacement field at the previous time step, which can be calculated during the forward problem solve. For the ALM, the required saddle-point matrices for the adjoint problem can also be assembled during the forward computation.

It is important to note that the system matrices arising in contact problems are non-symmetric in general. Consequently, when constructing the adjoint linear systems, Dirichlet boundary conditions must be applied after the transpose operation.

In case of frictionless contact all linearizations with respect to the previous timestep vanish and only the time steps evaluated in the objective function need to be considered in the adjoint system.

Finally, we have compared topology optimization results for frictionless and frictional contact formulations across several numerical examples. In the frictional cases, a directional dependence on the displacement history is observed, highlighting the importance of accounting for path-dependence in optimization problems involving frictional contact.

The examples presented in this publication consider several sources of nonlinear mechanics. This together with the density based topology optimization approach leads to non-convex optimization problems which may contain several minima. The evolutions of the objective functions reflect this complex setting. For example in the ironing problem, see Fig. 11, a local minimum is traversed. For clarity, we repeat the discussion given in Section 5.3. The convergence behavior can be explained by the used optimization algorithm and the post-processing of the design sensitivities. First, we use a version of the MMA [39,40] that does not enforce a monotonic reduction of the objective, even if the constraints are satisfied. Second, we follow the established work of [35,36] and filter the sensitivities to avoid checker-boarding, promote smooth design, and reduce mesh dependence. The observed convergence of the optimization problem does not indicate inaccurate sensitivities, nor instabilities related to solving the forward problem. In future studies, alternative optimization algorithms, such as the GCMMA, and density instead of sensitivity filtering could be studied.

Data availability

No data was used for the research described in the article.

CRediT authorship contribution statement

L. Rinderer: Writing – original draft, Visualization, Validation, Software, Methodology, Conceptualization; **A. Popp:** Writing – review & editing, Supervision, Resources, Investigation; **M. W. Gee:** Writing – review & editing, Supervision, Resources, Methodology, Funding acquisition, Conceptualization.

Declaration of competing interest

All authors declare that no conflicts of interest with respect to the submitted manuscript exist.

Acknowledgments

The authors gratefully acknowledge support through the Leibniz Rechenzentrum München (LRZ) of the Bavarian Academy of Sciences under contract pn34cu.

Supplementary material

Supplementary material associated with this article can be found, in the online version, at 10.1016/j.cma.2025.118507

References

[1] J.S. Jensen, P.B. Nakshatrala, D.A. Tortorelli, On the consistency of adjoint sensitivity analysis for structural optimization of linear dynamic problems, Struct. Multidiscip. Optim. 49 (5) (2014) 831–837. https://doi.org/10.1007/s00158-013-1024-4
[2] F. Fernandez, M.A. Puso, J. Solberg, D.A. Tortorelli, Topology optimization of multiple deformable bodies in contact with large deformations, Comput. Methods Appl. Mech. Eng. 371 (2020) 113288. https://doi.org/10.1016/j.cma.2020.113288
[3] M. Lawry, K. Maute, Level set topology optimization of problems with sliding contact interfaces, Struct. Multidiscip. Optim. 52 (6) (2015) 1107–1119. https://doi.org/10.1007/s00158-015-1301-5
[4] M. Lawry, K. Maute, Level set shape and topology optimization of finite strain bilateral contact problems, Int J Numer Methods Eng 113 (8) (2018) 1340–1369. https://doi.org/10.1002/nme.5582
[5] N. Strömberg, Topology optimization of orthotropic elastic design domains with mortar contact conditions, in: A. Schumacher, T. Vietor, S. Fiebig, K.-U. Bletzinger, K. Maute (Eds.), Advances in Structural and Multidisciplinary Optimization, Springer International Publishing, Cham, 2018, pp. 1427–1438. https://doi.org/10.1007/978-3-319-67988-4_108
[6] F. Sjövall, M. Wallin, D.A. Tortorelli, Shape optimization of hyperelastic structures subject to frictionless contact, Comput. Struct. 301 (2024) 107426. https://doi.org/10.1016/j.compstruc.2024.107426
[7] N. Strömberg, The influence of sliding friction on optimal topologies, in: G.E. Stavroulakis (Ed.), Recent Advances in Contact Mechanics: Papers Collected at the 5th Contact Mechanics International Symposium (CMIS2009), April 28–30, 2009, Chania, Greece, Springer Berlin Heidelberg, Berlin, Heidelberg, 2013, pp. 327–336. https://doi.org/10.1007/978-3-642-33968-4_20
[8] A. Myśliński, Level set method for optimization of contact problems, Eng. Anal. Bound. Elem. 32 (11) (2008) 986–994. https://doi.org/10.1016/j.enganabound.2007.12.008
[9] A. Myśliński, Piecewise constant level set method for topology optimization of unilateral contact problems, Adv. Eng. Software 80 (2015) 25–32. https://doi.org/10.1016/j.advengsoft.2014.09.020
[10] S. Stupkiewicz, J. Korelc, M. Dutko, T. Rodič, Shape sensitivity analysis of large deformation frictional contact problems, Comput. Methods Appl. Mech. Eng. 191 (33) (2002) 3555–3581. https://doi.org/10.1016/S0045-7825(02)00295-5
[11] S. Stupkiewicz, J. Lengiewicz, J. Korelc, Sensitivity analysis for frictional contact problems in the augmented lagrangian formulation, Comput. Methods Appl. Mech. Eng. 199 (33–36) (2010) 2165–2176. https://doi.org/10.1016/j.cma.2010.03.021
[12] C. Niu, W. Zhang, T. Gao, Topology optimization of elastic contact problems with friction using efficient adjoint sensitivity analysis with load increment reduction, Comput. Struct. 238 (2020) 106296. https://doi.org/10.1016/j.compstruc.2020.106296
[13] H. Kristiansen, K. Poulios, N. Aage, Topology optimization for compliance and contact pressure distribution in structural problems with friction, Comput. Methods Appl. Mech. Eng. 364 (2020) 112915. https://doi.org/10.1016/j.cma.2020.112915
[14] K. Poulios, Y. Renard, An unconstrained integral approximation of large sliding frictional contact between deformable solids, Comput. Struct. 153 (2015) 75–90. https://doi.org/10.1016/j.compstruc.2015.02.027
[15] H. Kristiansen, K. Poulios, N. Aage, Topology optimization of structures in transient impacts with Coulomb friction, Int. J. Numer. Methods Eng. 122 (18) (2021) 5053–5075. https://doi.org/10.1002/nme.6756
[16] T.A. Laursen, Computational Contact and Impact Mechanics: Fundamentals of Modeling Interfacial Phenomena in Nonlinear Finite Element Analysis ; with 6 Tables, Springer, Berlin, 1. ed., corr. 2. print edition, Berlin, 2002. https://doi.org/10.1007/978-3-662-04864-1
[17] P. Wriggers, Computational Contact Mechanics, Springer, Berlin ; New York, 2nd ed. edition, 2006. https://doi.org/10.1007/978-3-540-32609-0
[18] M.A. Puso, T.A. Laursen, A mortar segment-to-segment contact method for large deformation solid mechanics, Comput. Methods Appl. Mech. Eng. 193 (6–8) (2004) 601–629. https://doi.org/10.1016/j.cma.2003.10.010
[19] M.A. Puso, T.A. Laursen, A mortar segment-to-segment frictional contact method for large deformations, Comput. Methods Appl. Mech. Eng. 193 (45–47) (2004) 4891–4913. https://doi.org/10.1016/j.cma.2004.06.001
[20] S. Hüeber, B.I. Wohlmuth, A primal–dual active set strategy for non-Linear multibody contact problems, Comput. Methods Appl. Mech. Eng. 194 (27–29) (2005) 3147–3166. https://doi.org/10.1016/j.cma.2004.08.006
[21] A. Popp, M.W. Gee, W.A. Wall, A finite deformation mortar contact formulation using a primal–dual active set strategy, Int. J. Numer. Methods Eng. 79 (11) (2009) 1354–1391. https://doi.org/10.1002/nme.2614
[22] A. Popp, M. Gitterle, M.W. Gee, W.A. Wall, A dual mortar approach for 3D finite deformation contact with consistent linearization, Int. J. Numer. Methods Eng. 83 (11) (2010) 1428–1465. https://doi.org/10.1002/nme.2866
[23] M. Gitterle, A. Popp, M.W. Gee, W.A. Wall, Finite deformation frictional mortar contact using a semi-smooth Newton method with consistent linearization, Int. J. Numer. Methods Eng. 84 (5) (2010) 543–571. https://doi.org/10.1002/nme.2907
[24] M. Gitterle, A Dual Mortar Formulation for Finite Deformation Frictional Contact Problems Including Wear and Thermal Coupling, Ph.D. thesis, Technical University of Munich, 2012. https://nbn-resolving.org/urn:nbn:de:bvb:91-diss-20121120-1108639-1-7.
[25] S. Hüeber, Discretization Techniques and Efficient Algorithms for Contact Problems, Ph.D. thesis, Universität Stuttgart, Stuttgart, 2008. https://doi.org/10.18419/opus-4837
[26] M.A. Puso, A 3D mortar method for solid mechanics, Int. J. Numer. Methods Eng. 59 (3) (2004) 315–336. https://doi.org/10.1002/nme.865
[27] B.I. Wohlmuth, A mortar finite element method using dual spaces for the lagrange multiplier, SIAM J. Numer. Anal. 38 (3) (2000) 989–1012. https://doi.org/10.1137/S0036142999350929
[28] M. Hintermüller, K. Ito, K. Kunisch, The primal-dual active set strategy as a semismooth Newton method, SIAM J. Optim. 13 (3) (2002) 865–888. https://doi.org/10.1137/S1052623401383558
[29] S. Hüeber, G. Stadler, B.I. Wohlmuth, A primal-dual active set algorithm for three-dimensional contact problems with Coulomb friction, SIAM J. Sci. Comput. 30 (2) (2008) 572–596. https://doi.org/10.1137/060671061
[30] B. Yang, T.A. Laursen, X. Meng, Two dimensional mortar contact methods for large deformation frictional sliding, Int. J. Numer. Methods Eng. 62 (9) (2005) 1183–1225. https://doi.org/10.1002/nme.1222
[31] P. Michaleris, D.A. Tortorelli, C.A. Vidal, Tangent operators and design sensitivity formulations for transient non-linear coupled problems with applications to elastoplasticity, Int. J. Numer. Methods Eng. 37 (14) (1994) 2471–2499. https://doi.org/10.1002/nme.1620371408
[32] R. Alberdi, G. Zhang, L. Li, K. Khandelwal, A unified framework for nonlinear path-dependent sensitivity analysis in topology optimization, Int. J. Numer. Methods Eng. 115 (1) (2018) 1–56. https://doi.org/10.1002/nme.5794
[33] M. Zhou, G.I.N. Rozvany, The COC algorithm, part II: topological, geometrical and generalized shape optimization, Comput. Methods Appl. Mech. Eng. 89 (1–3) (1991) 309–336. https://doi.org/10.1016/0045-7825(91)90046-9

[34] M.P. Bendsøe, O. Sigmund, Topology Optimization: Theory, Methods, and Applications, Engineering Online Library, Springer, Berlin Heidelberg, 2nd ed., corrected printing edition, 2011. https://doi.org/10.1007/978-3-662-05086-6
[35] O. Sigmund, On the design of compliant mechanisms using topology optimization, J. Struct. Mech. 25 (4) (1997) 493–524. https://doi.org/10.1080/08905459708945415
[36] O. Sigmund, Morphology-based black and white filters for topology optimization, Struct. Multidiscip. Optim. 33 (4–5) (2007) 401–424. https://doi.org/10.1007/s00158-006-0087-x
[37] G.A. Holzapfel, Nonlinear Solid Mechanics: A Continuum Approach for Engineering, Wiley, Chichester ; New York, 2000.
[38] K. Svanberg, The method of moving asymptotes - a new method for structural optimization, Int. J. Numer. Methods Eng. 24 (2) (1987) 359–373. https://doi.org/10.1002/nme.1620240207
[39] K. Svanberg, Svanberg Matematisk Optimering Och IT AB, 2007, http://www.smoptit.se.
[40] K. Svanberg, MMA and GCMMA – Two methods for nonlinear optimization 1 (2007) 1–15.
[41] https://scholar.google.com/scholar_lookup?title=MMA%20and%20GCMMA-Two%20Methods%20for%20Nonlinear%20Optimization%2C%20Vol.%201&publication_year=2007&author=K.%20Svanberg.
[42] K.A. Fischer, P. Wriggers, Mortar based frictional contact formulation for higher order interpolations using the moving friction cone, Comput. Methods Appl. Mech. Eng. 195 (37–40) (2006) 5020–5036. https://doi.org/10.1016/j.cma.2005.09.025